

Effect of aromatics on in-flame soot in a jet fuelled small-bore optical diesel engine

Author:

Tian, Rongying

Publication Date:

2022

DOI:

<https://doi.org/10.26190/unsworks/24416>

License:

<https://creativecommons.org/licenses/by/4.0/>

Link to license to see what you are allowed to do with this resource.

Downloaded from <http://hdl.handle.net/1959.4/100709> in <https://unsworks.unsw.edu.au> on 2024-03-29

PLEASE TYPE	
The University of New South Wales Thesis/Dissertation Sheet	
Surname or Family name: Tian	
First name: Rongying	Other name/s:
Abbreviation for degree as given in the University calendar: MPhil	
School: Mechanical and Manufacturing Engineering	Faculty: Engineering
Title: Effect of aromatics on in-flame soot in a jet fuelled small-bore optical diesel engine	

Abstract 350 words maximum: (PLEASE TYPE)

This thesis investigates the effect of fuel aromatic content on soot distribution, particle morphology and internal structure inside the cylinder of an optically accessible engine. A set of custom-made jet fuels with 4%, 14% and 24% aromatic content are studied first with the 24% aromatics fuel (AR24) used for more detailed follow-up study of soot particle evolution along the flame development path. Time-resolved imaging of cool flame, OH* chemiluminescence signals and soot luminosity are performed to visualise the overall reaction development. Planar laser induced fluorescence imaging of HCHO and incandescence imaging of soot are also performed to obtain detailed understanding of reactions and soot distributions. Soot is analysed at a particle level. Using the thermophoresis-based particle sampling method, soot aggregates are collected from multiple in-bowl locations. Up to four soot sampling probes are installed on the piston-bowl wall with 60° spacing angles for simultaneous sampling from the same firing cycle. These sampling locations represent a jet-wall impingement point (JW), an up-swirl point (US), a down-swirl point 1 (DS1) and a down-swirl point 2 (DS2) along the sooting flame path. The subsequent transmission electron microscope (TEM) imaging of the collected soot particles enables structural analysis of soot particles as well as sub-nano-scale carbon layers. The results showed that the aromatic content has little impact on reactions and flame development among the tested fuels. However, the soot formation starts to occur earlier, and its growth rate is much higher for a higher aromatic fuel. The carbon-layer fringe analysis shows more mature, graphitised structures with higher aromatics at both formation-dominant and oxidation-dominant stages. For a selected AR24 fuel, the carbon-layer fringe analysis indicates continued oxidation during the flame penetration along the piston-bowl wall. Regarding the particle structure evolution, it is characterised by high formation of small aggregates at JW point, simultaneous aggregation and oxidation at US and DS1 point with the latter more prone to aggregation, and significant oxidation at DS2 point.

Declaration relating to disposition of project thesis/dissertation

I hereby grant to the University of New South Wales or its agents the right to archive and to make available my thesis or dissertation in whole or in part in the University libraries in all forms of media, now or here after known, subject to the provisions of the Copyright Act 1968. I retain all property rights, such as patent rights. I also retain the right to use in future works (such as articles or books) all or part of this thesis or dissertation.

I also authorise University Microfilms to use the 350 word abstract of my thesis in Dissertation Abstracts International (this is applicable to doctoral theses only).

.....
Signature

.....
Witness

.....
Date

The University recognises that there may be exceptional circumstances requiring restrictions on copying or conditions on use. Requests for restriction for a period of up to 2 years must be made in writing. Requests for a longer period of restriction may be considered in exceptional circumstances and require the approval of the Dean of Graduate Research.

FOR OFFICE USE ONLY

Date of completion of requirements for Award:

**THIS SHEET IS TO BE GLUED TO THE INSIDE FRONT COVER OF THE
THESIS**

Thesis submission for the degree of Master of Philosophy

Thesis Title and Abstract

Declarations

Inclusion of Publications
Statement

Corrected Thesis and
Responses

ORIGINALITY STATEMENT

☒ I hereby declare that this submission is my own work and to the best of my knowledge it contains no materials previously published or written by another person, or substantial proportions of material which have been accepted for the award of any other degree or diploma at UNSW or any other educational institution, except where due acknowledgement is made in the thesis. Any contribution made to the research by others, with whom I have worked at UNSW or elsewhere, is explicitly acknowledged in the thesis. I also declare that the intellectual content of this thesis is the product of my own work, except to the extent that assistance from others in the project's design and conception or in style, presentation and linguistic expression is acknowledged.

COPYRIGHT STATEMENT

☒ I hereby grant the University of New South Wales or its agents a non-exclusive licence to archive and to make available (including to members of the public) my thesis or dissertation in whole or part in the University libraries in all forms of media, now or here after known. I acknowledge that I retain all intellectual property rights which subsist in my thesis or dissertation, such as copyright and patent rights, subject to applicable law. I also retain the right to use all or part of my thesis or dissertation in future works (such as articles or books).

For any substantial portions of copyright material used in this thesis, written permission for use has been obtained, or the copyright material is removed from the final public version of the thesis.

AUTHENTICITY STATEMENT

☒ I certify that the Library deposit digital copy is a direct equivalent of the final officially approved version of my thesis.

Welcome to the Research Alumni Portal, Rongying Tian!

You will be able to download the finalised version of all thesis submissions that were processed in GRIS here.

Please ensure to include the **completed declaration** (from the Declarations tab), your **completed Inclusion of Publications Statement** (from the Inclusion of Publications Statement tab) in the final version of your thesis that you submit to the Library.

Information on how to submit the final copies of your thesis to the Library is available in the completion email sent to you by the GRS.

Thesis submission for the degree of Master of Philosophy

[Thesis Title and Abstract](#)[Declarations](#)[Inclusion of Publications
Statement](#)[Corrected Thesis and
Responses](#)

UNSW is supportive of candidates publishing their research results during their candidature as detailed in the UNSW Thesis Examination Procedure.

Publications can be used in the candidate's thesis in lieu of a Chapter provided:

- The candidate contributed **greater than 50%** of the content in the publication and are the "primary author", i.e. they were responsible primarily for the planning, execution and preparation of the work for publication.
- The candidate has obtained approval to include the publication in their thesis in lieu of a Chapter from their Supervisor and Postgraduate Coordinator.
- The publication is not subject to any obligations or contractual agreements with a third party that would constrain its inclusion in the thesis.

☒ The candidate has declared that their thesis has publications - either published or submitted for publication - incorporated into it in lieu of a Chapter/s. Details of these publications are provided below.

Publication Details #1

Full Title:	Effect of the jet fuel cetane number on combustion in a small-bore compression-ignition engine
Authors:	Zhang Y, Tian R, Meng S, Kook S, Kim KS, Kweon C-B
Journal or Book Name:	FUEL
Volume/Page Numbers:	292/120301
Date Accepted/Published:	22 January 2021
Status:	published
The Candidate's Contribution to the Work:	Validation, Investigation, Writing-review & editing.
Location of the work in the thesis and/or how the work is incorporated in the thesis:	Chapter 3 (Methodology)

Publication Details #2

Full Title:	Effect of jet fuel aromatics on in-flame soot distribution and particle morphology in a small-bore compression ignition engine
Authors:	Tian R, Zhang Y, Kook S, Kim KS, Kweon C-B
Journal or Book Name:	FUEL
Volume/Page Numbers:	305/121582
Date Accepted/Published:	26 July 2021
Status:	published
The Candidate's Contribution to the Work:	Methodology, Investigation, Validation.
Location of the work in the thesis and/or how the work is incorporated in the thesis:	Chapter 4

Publication Details #3

Full Title:	In-flame soot structure of a jet fuel with 24% aromatics in a small-bore optical compression-ignition engine
Authors:	Tian R, Kook S, Iijima K, Aizawa T, Kim KS, Kweon C-B
Journal or Book Name:	Combustion and Flame
Volume/Page Numbers:	
Date Accepted/Published:	
Status:	submitted
The Candidate's Contribution to the Work:	Methodology, Investigation, Validation.
Location of the work in the thesis and/or how the work is incorporated in the thesis:	Chapter 5

Publication Details #4

Full Title:	On-grid location-by-location variations of transmission electron microscope imaged in-flame soot particles in a small-bore diesel engine
Authors:	Tian R, Zhang Y, and Kook
Journal or Book Name:	22nd Australasian Fluid Mechanics Conference AFMC2020
Volume/Page Numbers:	
Date Accepted/Published:	1 September 2021
Status:	published
The Candidate's Contribution to the Work:	Methodology, Investigation, Validation.
Location of the work in the thesis and/or how the work is incorporated in the thesis:	Chapter 3 (Methodology)

Candidate's Declaration



I confirm that where I have used a publication in lieu of a chapter, the listed publication(s) above meet(s) the requirements to be included in the thesis. I also declare that I have complied with the Thesis Examination Procedure.



Effect of aromatics on in-flame soot in a jet fuelled small-bore optical diesel engine

Rongying Tian

A thesis in fulfilment of the requirements for the degree of
Master of Philosophy

School of Mechanical and Manufacturing Engineering
The University of New South Wales

May 2022

Originality Statement

‘I hereby declare that this submission is my own work and to the best of my knowledge it contains no materials previously published or written by another person, or substantial proportions of material which have been accepted for the award of any other degree or diploma at UNSW or any other educational institution, except where due acknowledgement is made in the thesis. Any contribution made to the research by others, with whom I have worked at UNSW or elsewhere, is explicitly acknowledged in the thesis. I also declare that the intellectual content of this thesis is the product of my own work, except to the extent that assistance from others in the project’s design and conception or in style, presentation and linguistic expression is acknowledged.’

Signed

Date

Acknowledgements

The completion of my two-year MPhil study and entire thesis would not happen without the help from the surrounding people, and my feelings are beyond words.

First, I would like to express my thanks to my supervisor Prof. Shawn Kook. Thank you for providing me the opportunity to know the forefront of the industry and work with this professional research group. I am grateful to be your student and I really appreciate your time for teaching me the skills, inspiring me to think about things from different perspectives and supporting my study with patience. You are a role model for me in academics. I also would like to thank my co-supervisor Dr. Qing Nian Chan for supporting me all the time.

To my parents Prof. Yongjiang Tian and Lijun Shi, thank you for always being by my side and supporting my decisions when I face difficulties. You gave me the best, so I have no regrets in every step. Also, a special thanks to my close friend Zimu Guo – thank you for your care and companionship all the time.

Special thanks to Dr. Yilong Zhang and Dr. Lingzhe Rao for guiding me in every detail and working closely with me at the initial stage of my study. I cannot complete my research smoothly without the help from you. I will never forget the time spent with you. To Dr. Dongchan Kim and the lab officer Bryce Edmonds - thank you for taking care of me in dealing with the technical and mechanical problems. I admire your flexible thinking and professional attitude. Also, I would like to thank my good friends Xinyu Liu, Jinxin Yang, and Yuwei Lu for sharing your experience and knowledge with me not only in academics but also in daily life. You are my true friends beyond work relationships, and it is fantastic to study with you. A special thanks go to Emily Ou, thank you for

enlightening me when I was depressed and confused. You make my study life relaxed and pleasant.

These two years of study are unforgettable to me, it has been both happy and difficult. I wish everyone a bright future.

Table of Contents

Originality Statement.....	i
Acknowledgements.....	ii
Table of Contents	iv
Abstract.....	vi
List of figures	viii
List of tables.....	xi
List of abbreviations	xii
List of publications.....	xiii
Chapter 1. Introduction.....	1
1.1 Research aim and scope.....	2
Chapter 2. Literature review	4
2.1 Diesel combustion process	4
2.2 Soot process	6
2.2.1 Soot formation and oxidation fundamentals	6
2.2.2 In-flame soot structure	8
2.3 Effect of aromatic hydrocarbons on combustion process	10
2.4 Effect of aromatic hydrocarbons on soot	11
2.5 Research gaps	13
Chapter 3. Methodology	15
3.1 Optical diesel engine	15
3.2 Fuel properties.....	19
3.3 High-speed imaging.....	20

3.4 Planer laser induced fluorescence/incandescence and the image selection method.....	22
3.5 Multi-location in-flame soot sampling.....	24
3.6 TEM imaging and post-processing	25
Chapter 4. Aromatics effect on in-flame soot distribution and morphology	29
4.1 Pressure traces, heat release rate and high-speed images	30
4.2 Planar laser-based images	35
4.3 Soot particle structure and statistical analysis	39
Chapter 5. Understanding of soot structure evolution of jet fuel with 24% aromatics	44
5.1 In-cylinder pressure and soot luminosity images.....	45
5.2 Planar laser induced incandescence (PLII) images.....	49
5.3 Soot particle morphology analysis.....	50
5.4 Soot internal structure analysis	55
Chapter 6. Conclusion	59
6.1 Future work	61
Reference.....	63

Abstract

This thesis investigates the effect of fuel aromatic content on soot distribution, particle morphology and internal structure inside the cylinder of an optically accessible engine. A set of custom-made jet fuels with 4%, 14% and 24% aromatic content are studied first with the 24% aromatics fuel (AR24) used for more detailed follow-up study of soot particle evolution along the flame development path. Time-resolved imaging of cool flame, OH* chemiluminescence signals and soot luminosity are performed to visualise the overall reaction development. Planar laser induced fluorescence imaging of HCHO and incandescence imaging of soot are also performed to obtain detailed understanding of reactions and soot distributions. Soot is analysed at a particle level. Using the thermophoresis-based particle sampling method, soot aggregates are collected from multiple in-bowl locations. Up to four soot sampling probes are installed on the piston-bowl wall with 60° spacing angles for simultaneous sampling from the same firing cycle. These sampling locations represent a jet-wall impingement point (JW), an up-swirl point (US), a down-swirl point 1 (DS1) and a down-swirl point 2 (DS2) along the sooting flame path. The subsequent transmission electron microscope (TEM) imaging of the collected soot particles enables structural analysis of soot particles as well as sub-nano-scale carbon layers. The results showed that the aromatic content has little impact on reactions and flame development among the tested fuels. However, the soot formation starts to occur earlier, and its growth rate is much higher for a higher aromatic fuel. The carbon-layer fringe analysis shows more mature, graphitised structures with higher aromatics at both formation-dominant and oxidation-dominant stages. For a selected AR24 fuel, the carbon-layer fringe analysis indicates continued oxidation during the flame penetration along the piston-bowl wall. Regarding the particle structure evolution, it is characterised

by high formation of small aggregates at JW point, simultaneous aggregation and oxidation at US and DS1 point with the latter more prone to aggregation, and significant oxidation at DS2 point.

List of figures

Figure 2.1 The internal logical connection diagram of literature review (Chapter 2).....	4
Figure 2.2: Illustration of LTR and HTR [17]	5
Figure 2.3: The decomposition of LTR and HTR [17]	5
Figure 2.4 Soot particles formation process [23]	6
Figure 2.5: Example of liquid-like particles under TEM [23]	6
Figure 2.6: Soot aggregates size distribution at varying fuel injection pressure (FIP) [42]	8
Figure 2.7: Fringe separation of flame core and periphery soot [36]	8
Figure 2.8: Heat release rate of varying diesel and benzene blends at fixed fuel injection timing [48]	10
Figure 2.9: Heat release rate of varying M-XYL and heptane blends at fixed fuel injection timing [54]	10
Figure 2.10: Flame temperature of varying fuel aromatics [65]	12
Figure 2.11: Simulation results of soot formation and oxidation for fuels with 15% and 30% toluene [66]	12
Figure 3.1: Single-cylinder optical diesel engine assembly.....	16
Figure 3.2: Sketch of the optical compression ignition engine, optical/laser-based imaging diagnostics setup and in-flame soot sampling system. Example images of the combined HCHO-PLIF and the soot-PLII signals are presented in the middle. The soot probes installed at location A and B and two different types of standard and lacy transmission electron microscope (TEM) grids used for soot structure analysis are shown on the top- right corner	16
Figure 3.3: The first signal frame of OH* chemiluminescence images from 15 cycles for AR14 fuel. The bottom plot shows the variation level of the start timing of OH* chemiluminescence signal.....	20
Figure 3.4: Individual soot-PLII images from 20 cycles for AR24 at 10mm laser plane as an example (10°C aTDC), the ensemble averaged image of 20 cycles (blue frame), and the selected image (yellow frame). The cross-correlation coefficients are plotted at bottom, and the selected image has the highest coefficient (0.720) as marked with yellow box.....	22

Figure 3.5: Standard TEM images taken at 30 different on-grid locations for the soot samples at location A and location B (top), and the variation of soot aggregate radius of gyration and primary particle diameter with increasing number of processed TEM images (bottom) for the location A and location B. The results are presented for AR24 fuel....	26
Figure 3.6: Soot particles morphology and internal structure analysis	27
Figure 3.7: High resolution TEM (HR-TEM) images taken at 10 different on-grid locations for the soot samples at location A and location B (top), and the variation of soot primary particles fringe length and fringe tortuosity with an increase in processed HR-TEM images (bottom) for the location A and location B. The results are presented for AR24 fuel	28
Figure 4.1 Illustration of in-bowl soot sampling locations	29
Figure 4.2: In-cylinder pressure traces of all measured individual cycles and their ensemble average (top) and the calculated apparent heat release rate (aHRR) traces for AR04, AR14 and AR24 fuels. The duration of pilot and main injections is illustrated on the aHRR traces.....	30
Figure 4.3: Cool flame chemiluminescence and OH* chemiluminescence images of a selected cycle for AR04, AR14 and AR24 fuels. Shown at the right are the OH* signal intensity profiles and the CoVs of the first detected OH* chemiluminescence timing and the maximum timing	32
Figure 4.4: High-speed soot luminosity images of a selected cycle for AR04, AR14 and AR24 fuels	34
Figure 4.5: HCHO-PLIF images of AR04, AR14 and AR24 fuels during the first-stage ignition phase at 8 mm and 10 mm below the cylinder head.....	36
Figure 4.6: Soot-PLII images during the sooting phase of AR04, AR14 and AR24 fuels at 8 mm and 10 mm laser below the cylinder head.....	37
Figure 4.7: High resolution TEM images of soot primary particles sampled at location A and location B for AR04, AR14 and AR24 fuels. The dashed lines and circles illustrate the shell and core regions of the soot primary particles. On the leftmost column, processed carbon-layer fringes are shown using white lines	40
Figure 4.8: Probability density functions of carbon-layer fringe length (top) and fringe tortuosity (bottom) for soot primary particles of AR04, AR14 and AR24 fuels at location A (left) and location B (right) with the 95% confidence error range.....	40
Figure 4.9: The standard TEM images showing soot aggregates sampled at location A and location B for AR04, AR14 and AR24 fuels	42
Figure 4.10: Probability density functions of soot primary particle diameter (d_p , left), aggregate radius of gyration (R_g , middle) and aggregate fractal dimension (df , right) for	

AR04, AR14 and AR24 fuels at location A (top) and location B (bottom) with 95% confidence error range.....	42
Figure 5.1: Illustration of in-bowl soot sampling locations	44
Figure 5.2: In-cylinder pressure, apparent heat release rate and selected high-speed soot luminosity images of a single injection condition for diesel and AR24 fuels. For AR24, the images are shown for both with and without the soot sampling probes	46
Figure 5.3: Selected planar laser induced incandescence (PLII) images of diesel and AR24 fuel with a single injection. The PLII images are shown for the different laser planes below the cylinder head	50
Figure 5.4: Example TEM images of the four sampling locations for each of diesel and AR fuels. A 30k TEM magnification is used for the soot aggregate number counting with the mean value plotted with error margins of 95% confidence	51
Figure 5.5: Size distribution of the soot aggregate radius of gyration and primary particles of the four sampling locations. The results are shown for diesel (left) and AR24 fuel (right). The estimated fractal dimension is shown at the bottom.....	54
Figure 5.6: Example HR-TEM images of a soot primary particle and overlaid concentricity colormap for four sampling locations of AR24 fuel. The frequency plot of the concentricity calculated from five soot primary particles is shown at the bottom....	56
Figure 5.7: Example HR-TEM images of AR24 fuel at varied sampling locations (top). Shown in the middle are the corresponding carbon-layer fringes. The PDF profiles of the fringe length, tortuosity and separation are presented at the bottom row	57

List of tables

Table 3.1 Engine specification and operating conditions	17
Table 3.2 Fuel chemical composition and physical properties	18
Table 4.1 Engine operating conditions for varying aromatic fuel study	28
Table 5.1 Engine operating conditions for soot evolution study	43

List of abbreviations

$^{\circ}\text{CA}$	Crank angle degree
$^{\circ}\text{CA aTDC}$	Crank angle degree after top dead centre
$^{\circ}\text{CA bTDC}$	Crank angle degree before top dead centre
aHRR	Apparent heat release rate
aEOI	After end of injection
aSOI	After start of injection
CCD	Charge coupled device
CMOS	Complementary metal-oxide semiconductor
CoV	Coefficient of variation
d_p	Primary particle diameter
D_f	Aggregate fractal dimension
ICCD	Intensified charge-coupled device
L_f	Fringe length
OH-PLIF	Planar laser-induced fluorescence of hydroxyl
PAH	Polycyclic aromatic hydrocarbon
PLII	Planar laser induced incandescence
R_g	Aggregate radius of gyration
TEM	Transmission electron microscope
T_f	Fringe tortuosity

List of publications

A total of 3 journal and 1 conference papers have been produced during my MPhil candidature. They are included in this thesis in methodology chapter (Chapter 3) and results and discussion chapters (Chapter 4 and 5).

Journal paper

- 1) Chapter 3 (Methodology): Zhang Y, Tian R, Meng S, Kook S, Kim KS, Kweon C-B, “Effect of the jet fuel cetane number on combustion in a small-bore compression-ignition engine”. *Fuel* 2021;292:120301. <https://doi.org/10.1016/j.fuel.2021.120301>
- 2) Chapter 4: Tian R, Zhang Y, Kook S, Kim KS, Kweon C-B. “Effect of jet fuel aromatics on in-flame soot distribution and particle morphology in a small-bore compression ignition engine”. *Fuel* 2021;305:121582. <https://doi.org/10.1016/j.fuel.2021.121582>
- 3) Chapter 5: Tian R, Kook S, Iijima K, Aizawa T, Kim KS, Kweon C-B. “In-flame soot structure of a jet fuel with 24% aromatics in a small-bore optical compression-ignition engine”. *Combustion and Flame*, *in review*

Peer-reviewed conference paper

- 1) Tian R, Zhang Y, and Kook S, “On-grid location-by-location variations of transmission electron microscope imaged in-flame soot particles in a small-bore diesel engine”. 22nd Australasian Fluid Mechanics Conference AFMC2020, Brisbane, Australia, 7-10 December 2020.

Chapter 1.

Introduction

Small-bore compression ignition (CI) engines with about 75~85 mm bore size are ubiquitous with a wide range of applications. Due to recent diesel emissions scandal and the current industry trend towards electric and electrified hybrid vehicles, the diesel passenger car market share has been shrunk [1]. However, it still marks 36% in Europe [2] and in some countries, its market share increases due to high popularity of diesel Ute/SUVs [3]. It is widely used as a mobile power generator that provides electricity to various outdoor events and emergency backup power to buildings and trains [4]. They are currently used to charge battery electric vehicles in factory stores and in remote areas. Using jet fuel in the fuel tank, they are also used in class II unmanned aerial vehicles and some military ground vehicles.

Soot emissions have long been one of the most problematic issues of compression ignition engines as their negative impacts on human health are well known [5]. Since the in-cylinder soot reduction is an immediate solution [6,7], many researchers have optimised fuel injection strategies to produce air-fuel mixtures and flame temperature favoured for lower soot emissions. For instance, increasing injection pressure, splitting the main injection and adjusting injection timings are used as an effective means to inhibit soot production while enhancing soot oxidation [8,9]. To further reduce engine-out soot emissions, optimising the fuel is also considered because, as an incomplete combustion product, the soot emission is directly related to the fuel chemical composition [7,10].

Among numerous components, aromatic hydrocarbons have been extensively studied since they are original contents in petroleum with very high sooting propensity [11,12]. For example, polycyclic aromatic hydrocarbons (PAHs), major subsets of the aromatic hydrocarbons, are well known precursors to the soot formation [7,13,14].

1.1 Research aim and scope

This MPhil thesis aims to enhance fundamental understanding about soot structures in a running small-bore CI engine. An innovative soot sampling method is used in conjunction with optical/laser-based imaging diagnostics performed in an optically accessible engine.

In the first part of this thesis (Chapter 4), custom-made, surrogate jet fuels with varied aromatic content of 4%, 14% and 24% are studied while the other fuel properties are kept unchanged. This is to systematically investigate the aromatics effects on soot. Time-resolved imaging of cool flame, OH*chemiluminescence signals and soot luminosity are performed to visualise the overall reaction development. Planar laser induced fluorescence imaging of HCHO and incandescence imaging of soot are also performed to obtain detailed understanding of reactions and soot distributions. Soot is analysed at a particle level. Using the thermophoresis-based particle sampling method, soot aggregates are collected from multiple in-bowl locations. The subsequent transmission electron microscope (TEM) imaging of the collected soot particles enables structural analysis of soot particles as well as sub-nano-scale carbon layers.

In the second part of the study (Chapter 5), an upgraded multi-location soot sampling method is developed and implemented in a small-bore optical compression ignition engine, which enables sampling of soot from varied stages of combustion as the multiple

probes are located along the flame development path. This study is conducted using a surrogate jet fuel with 24% aromatics (AR24). Four soot sampling probes are installed on the piston-bowl wall with 60° spacing angles for simultaneous sampling from the same firing cycle. These sampling locations represent a jet-wall impingement point (JW), an up-swirl point (US), a down-swirl point 1 (DS1) and a down-swirl point 2 (DS2) along the sooting flame development path identified by high-speed soot luminosity images and planar laser induced incandescence (PLII) images. The TEM images of the sampled soot particles are post processed for the analysis of morphology, concentricity and internal structure.

Chapter 2.

Literature review

The previous literature regarding the diesel combustion, soot process and how they are impacted by fuel aromaticity was reviewed. The scope and the internal logic of this literature review part is illustrated in Figure 2.1.

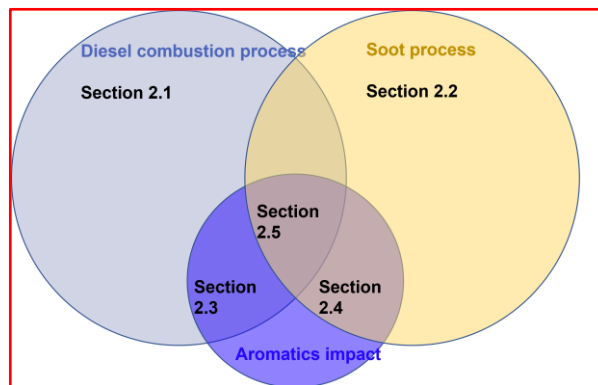


Figure 2.1 The internal logical connection diagram of literature review (Chapter 2).

2.1 Diesel combustion process

The diesel combustion within compression ignition (CI) engines involves a two-stage ignition process, which is the result of the oxidation of large alkanes [15]. From the conceptual model study of the diesel engine, the first stage low-temperature reaction (LTR) is followed by the second-stage high-temperature reaction (HTR) as shown in Figure 2.1 [16,17]. As the LTR induces the temperature and pressure increase, it appears as a small heat release bump prior to the start of combustion and the main heat release from pre-mixed combustion [17–19]. The LTR is known to commence with the

decomposition of ketohydroperoxide (KHP), which is a relatively stable isomerisation product of fuel [17,20]. As the temperature exceeds 800 K, the chain branching stops and the KHP starts to turn into several other species such as formaldehyde (HCHO) and hydrogen peroxide (H₂O₂) as shown in Figure 2.2 [17]. Cool flame chemiluminescence imaging is used to visualise the spatial location of LTR through capturing the signal from its resultant (*i.e.* HCHO radicals) [16].

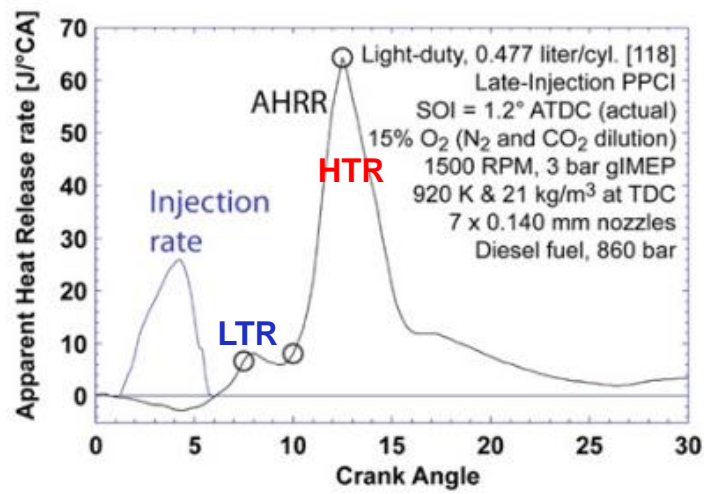


Figure 2.2: Illustration of LTR and HTR from [17]

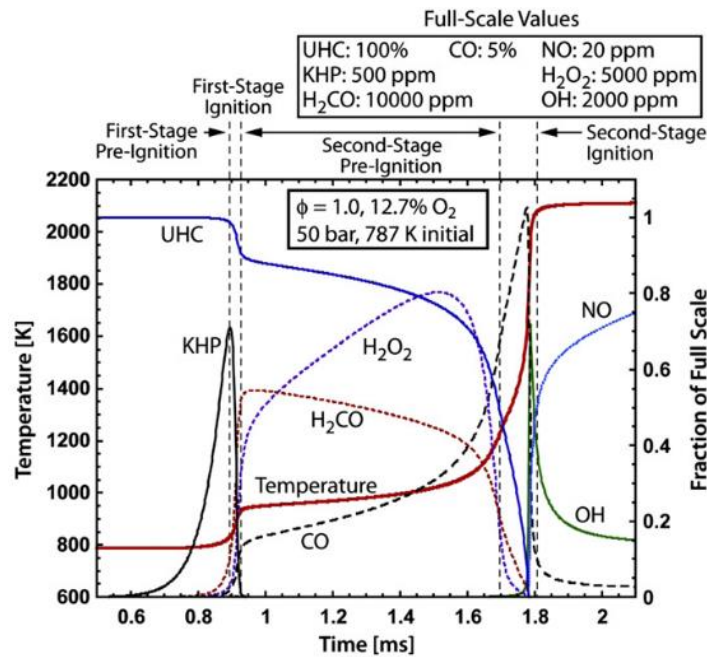


Figure 1.3: The decomposition of LTR and HTR [17]

The LTR is followed by the HTR as the second stage ignition of the fuel-air mixture occurs during which a large amount of heat is released and the peak heat release rate is measured [21,22]. Figure 2.2 shows the HTR occurring at the temperature of over 1000 K, which involves the consumption of HCHO, the decomposition of H_2O_2 and the formation of OH radicals [17,20]. These lead to an increased oxidation rate and thereby causing a significant rise in temperature [17]. Due to these reaction chemistries, HCHO and OH radicals are regarded as a good marker of LTR and HTR.

2.2 Soot process

2.2.1 Soot formation and oxidation fundamentals

Soot formation involves complex physical processes and chemical reactions [23]. From open flame burners and high-pressure constant-volume combustion chambers (CVCC)

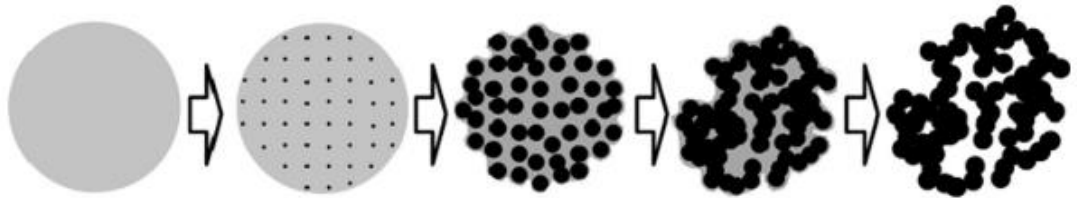


Figure 2.4 Soot particles formation process [23]

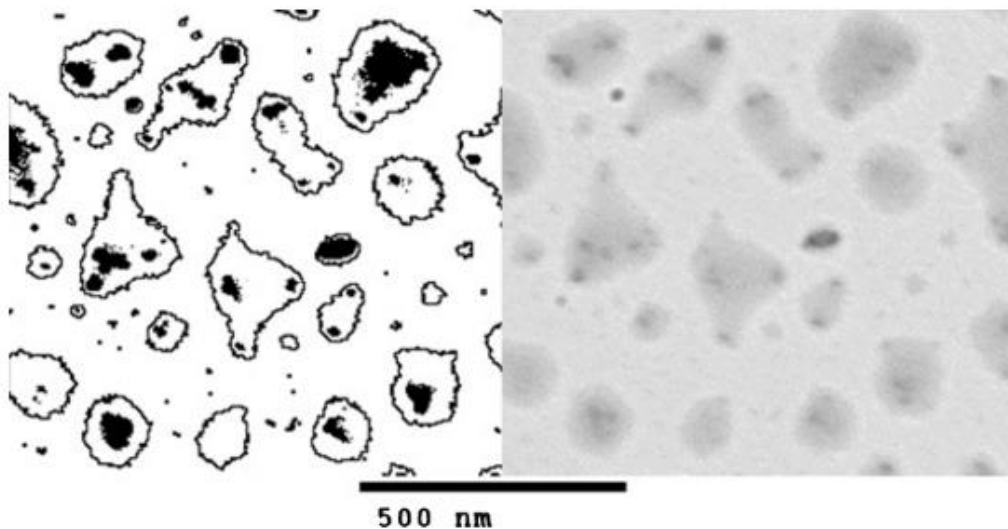


Figure 2.5: Example of liquid-like particles under TEM [23]

[23,24], soot was found to form from precursors such as polycyclic aromatic hydrocarbons (PAH) and acetylene (C_2H_2) due to fuel pyrolysis in a high-temperature environment [23,25,26]. In the early stage, a large amount of PAHs cluster together to form transparent and liquid-like nascent soot particles as shown in Figure 2.3 [23,24,27–30]. As the temperature increases, the dark nuclei starts to form and grow on the surface of the liquid-like particles, and the subsequent surface growth results in the formation of spherical primary particles [23,27], as illustrated in Figure 2.4. Through the visualisation of carbon-layer internal structures at sub nano scales, soot particles show highly disordered carbon fringes and undefined core surrounded by highly ordered shell – *i.e.* core-shell structures [26,27]. The aggregation of these spherical primary particles leads to the formation of nascent aggregates, which are carbonised to become more mature soot aggregates during the oxidation process [24]. Concurrently, the soot oxidation causes the breakdown of soot aggregates into smaller particles/aggregates with more compact structures [31,32].

Notably, the soot oxidation process is always accompanied by the formation, hence, the PAHs inside primary particles are experiencing carbonisation and aromatisation within high-temperature flames to form graphitised outer shell structure [33]. Meanwhile, the nascent aggregates proceed to become more mature during the oxidation process by involving the dehydrogenation at a high flame temperature [26,27,34,35]. The oxidation is shown in the soot internal structures. For instance, high-resolution TEM (HR-TEM) images showed smaller fringe-to-fringe gap, increased carbon-layer fringe length and less curved fringes [27]. The concentricity analysis of carbon-layer fringes also showed that soot oxidation could convert the single-core structure into multi-core structures [36].

2.2.2 In-flame soot structure

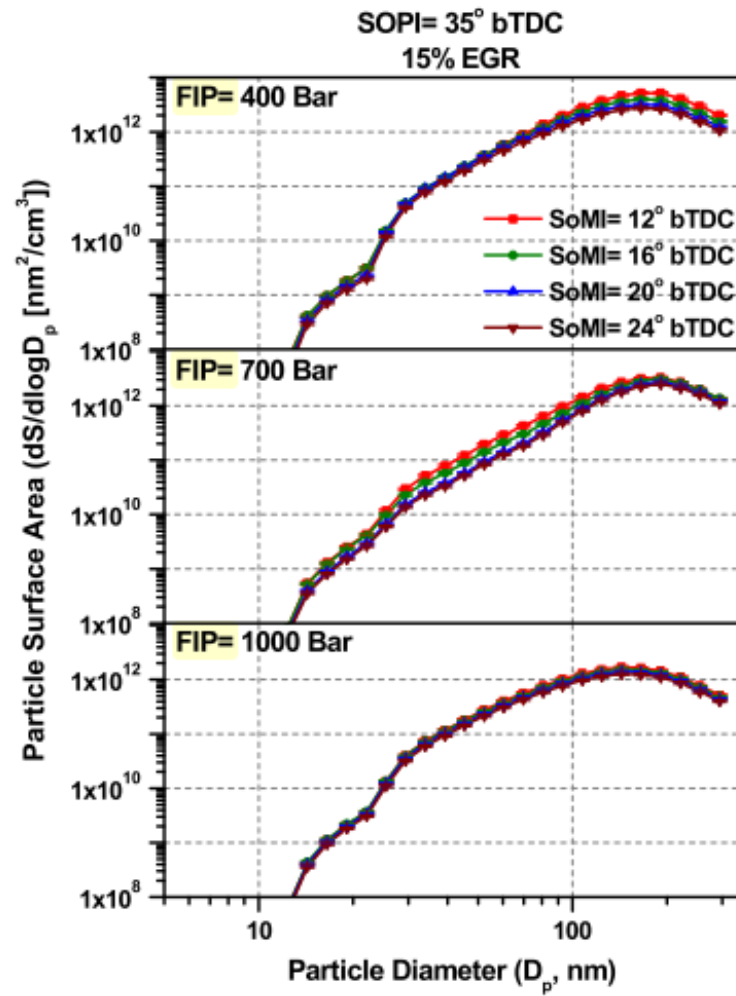


Figure 2.6: Soot aggregates size distribution at varying fuel injection pressure (FIP) [42]

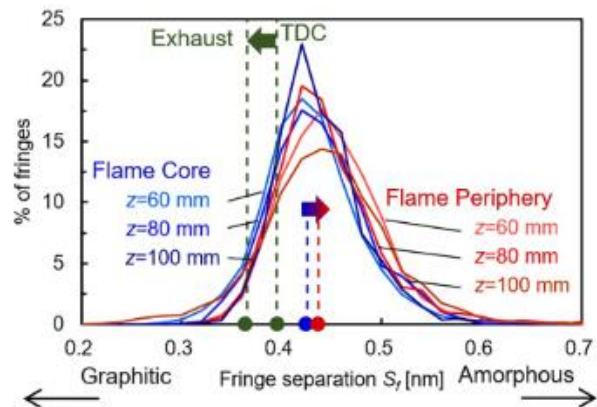


Figure 2.7: Fringe separation of flame core and periphery soot [36]

Reducing harmful soot emissions from the small-bore CI engine has been a main research goal, which requires a good understanding of soot structures (e.g. [37–39]) . Therefore, the soot particle structure has also been studied in a CI engine environment. Previous experimental studies applied thermophoretic soot sampling to the engine exhaust pipe [40–42]. With variations in engine operating conditions, the engine-out soot particles showed a significant change in structures. For example, previous studies reported that soot particles at higher engine loads tend to show more compact aggregate structures [40], which is related to higher temperature conditions and thus enhanced soot oxidation. Also, the late fuel injection timing leads to increased soot aggregate number counts while the aggregates become more stretched chain-like structures [41]. This is due to the lowered flame temperature and thus reduced soot oxidation reaction. On the other hand, increased fuel injection pressure leads to smaller soot primary particles and aggregates through enhanced mixing as shown in Figure 2.5 [42].

Given the engine-out soot shows only the net result of complex formation and oxidation processes occurring inside the cylinder of the engine [7], the in-flame soot sampling was also performed in running CI engines [43]. Previous studies [44,45] showed a large amount of small soot aggregates firstly form in the region where the sooting flame impinges on the piston-bowl wall. The soot aggregate size increases due to the aggregation occurring within the flame travelling along the bowl wall [43,46]. At a later stage, the soot oxidation causes the aggregates to be smaller and more compact [45] while the carbon-layer structures show a clear sign of graphitisation [43]. However, a recent study [36] compared the soot particles sampled from the flame core and periphery regions and found a direct opposite trend such that the flame core soot with limited oxidation has a narrower carbon-layer fringe gap than that of more oxidated soot sampled from the flame periphery as shown in Figure 2.6. This suggests that more graphitised soot with

narrower carbon-layer fringe gap does not necessarily mean more oxidised soot, but it could be that the flame core soot only survived longer and was sampled in the later stage of combustion. Therefore, it is crucial to sample soot particles from varied in-flame locations before their oxidation status is judged from TEM images.

2.3 Effect of aromatic hydrocarbons on combustion process

Previous studies reported that fuel aromatics impacts both LTR and HTR of diesel combustion [47–52], which varies due to aromatic types [47,53]. A previous study

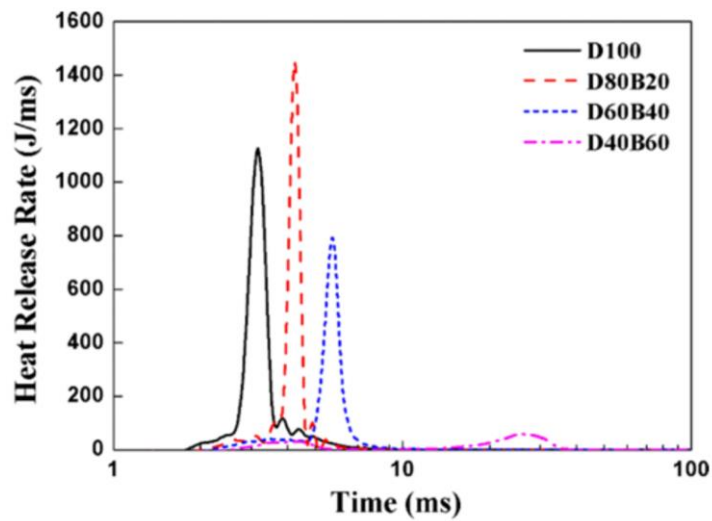


Figure 2.8: Heat release rate of varying diesel and benzene blends at fixed fuel injection timing [48]

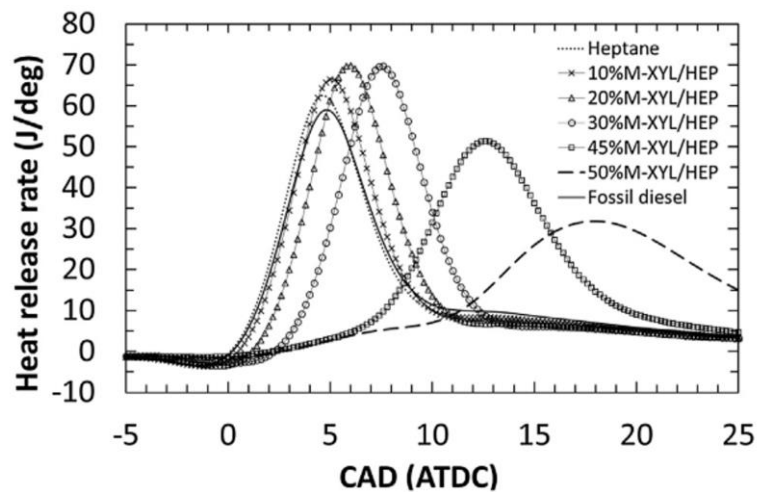


Figure 2.9: Heat release rate of varying M-XYL and heptane blends at fixed fuel injection timing [54]

conducted in an open flame burner showed that adding n-propylbenzene (n-PB) as a selected aromatic in n-dodecane (*i.e.* alkyl) reduces LTR as the n-PB reacts with OH radicals to interfere the chain branching and alkyl oxidation [53]. However, an opposite trend was observed when experiments were conducted with toluene, another widely used aromatic, in a high-pressure combustion chamber with the addition of toluene causing longer lasting cool flame chemiluminescence signals [47]. The mixed trends of aromatics effects were also found in the HTR. The n-PB research mentioned above reported that higher aromatics leads to increased OH radicals and thus HTR was enhanced [53]. However, when benzene was used, the peak heat release rate was increased only up to 20% benzene addition before it decreased dramatically at a higher benzene proportion [48]. Similarly, m-xylene tested in a CI engine showed increased peak heat release rate only up to 30% m-xylene addition [54]. Given these mixed conclusions from previous studies, a systematic experimental research of fuel aromatics and their influence on engine combustion is required.

2.4 Effect of aromatic hydrocarbons on soot

Previous studies investigated the mechanism of soot formation and its dependency on aromatics [12,13,55–58]. In an open flame burner, a higher soot concentration and formation rate was measured when benzene, an aromatic hydrocarbon, was added to the fuel due to increased formation of large aromatics and PAHs within the flame [59]. The increased soot emissions due to higher aromatics were also reported in diesel engines [60,61]. Consistent with the findings made from the open flame burners, the increased engine-out soot emissions were suggested as a result of enhanced soot initial inception and increased soot formation rate [51,62], which are related to PAHs produced in a rich benzene-ring environment [62,63]. It is explained that heavy aromatic hydrocarbons are hard to decompose and can survive in high temperature flames for a long time during

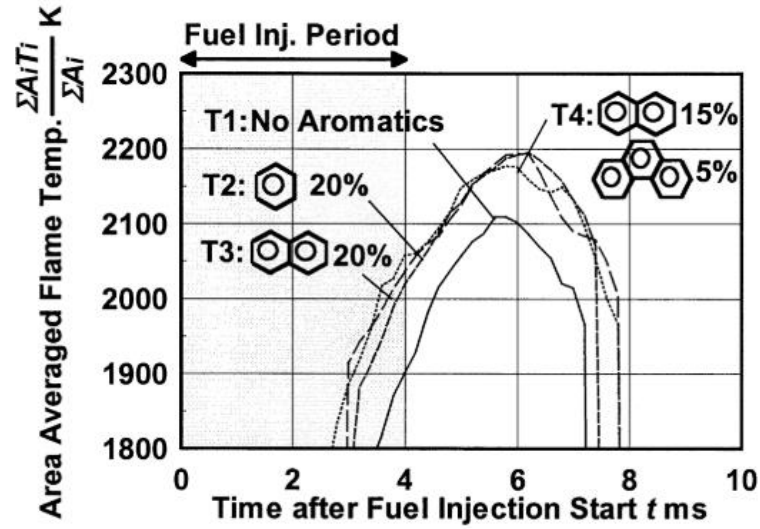


Figure 2.10: Flame temperature of varying fuel aromatics [65]

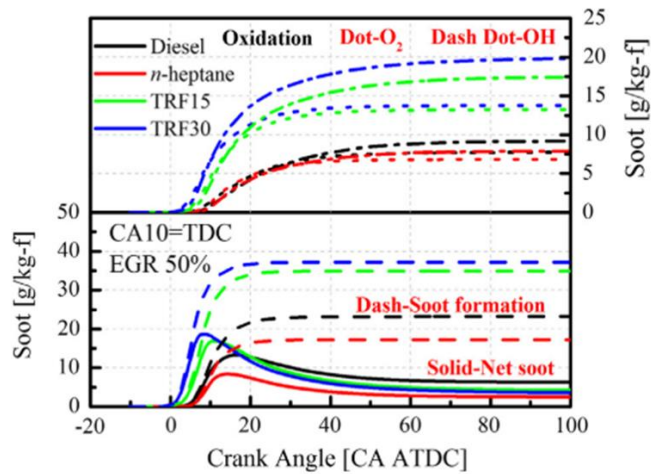


Figure 2.11: Simulation results of soot formation and oxidation for fuels with 15% and 30% toluene [66]

which they cause high soot inception [62]. While the increased aromatics in fuel makes a direct impact on increased soot formation, a higher amount of aromatics can result in increased flame temperature as shown in Figure 2.9 [64,65], which also causes the increased soot formation rate [6,7]. However, the increased flame temperature would also enhance the soot oxidation. Numerical modelling studies [66,67] provided additional insights such that higher toluene proportions in the fuel result in increased soot formation as well as enhanced oxidation due to increased temperature [65] as shown in Figure 2.10.

This means the increased soot emissions for higher aromatic fuels occurred because the increased soot formation outperformed the increased soot oxidation.

2.5 Research gaps

Although a positive relationship between aromatic content and soot emission is clear, there still is a concern that the aromatics alter other fuel physical properties including density, viscosity and ignition quality, which also makes a significant influence on soot formation [68,69]. For example, an increase in toluene leads to higher fuel density, lower viscosity and ignition quality [7,70,71]. Since higher density fuels lead to increased soot formation on account of lower mixing rate and higher locally rich mixtures [40], the soot increase is not solely due to increased aromatics. On the other hand, lower fuel viscosity enhances the atomisation and lower ignition quality extends the ignition delay and thereby increasing the premixed combustion and lowering the soot formation [47,72]. Therefore, the increased soot emissions due to higher aromatics might be underestimated. How higher aromatics in the fuel impacts the soot particle structures were previously investigated. The soot particles in the exhaust stream showed larger size [73], which is related to enhanced growth of particle surface and stronger soot aggregation caused by additional aromatic hydrocarbons [45]. However, the influence of aromatics on the soot particle morphology variations within the flame in a running engine is currently unknown. Given the exhaust soot is a result of complex soot processes occurred inside the cylinder of the engine, this leaves a significant knowledge gap. The first part of this MPhil thesis aims to bridge this gap. The preliminary hypothesis for this part is: the increased fuel aromaticity leads to higher in-flame soot formation and a more complex soot structure. This will be revealed in later Chapter 4.

While the previous studies provided useful information about the soot particle evolution inside the cylinder of the engine, the soot sampling method was limited at a fixed point and therefore the soot particles were sampled from different engine cycles before the results from different soot sampling locations (or the in-flame locations) are compared. One study achieved simultaneous soot sampling from three different locations by placing the probes in the jet-jet interaction location and its up-swirl and down-swirl locations along the piston-bowl wall [74]. However, a two-hole nozzle was used and thus no soot sampling experiment was conducted for a single flame from multiple in-flame locations simultaneously. Another missing link for the application of soot particle research to small-bore CI engines is lack of jet fuels. Fuel molecular structures are known to make a significant impact on soot particle structures. For example, methyl decanoate, an oxygenated biodiesel surrogate fuel, showed relatively smaller aggregate and primary particle size compared to those of a conventional diesel fuel [43,46,75]. Also, the internal carbon-layer structures are more compact and graphitised [76,77]. Bridging these two gaps – *i.e.* jet fuel soot structure evolution achieved through simultaneous multi-point soot sampling for a single jet flame – is the main motivation of the second part of this MPhil thesis. Based on the previous literature, the hypothesis for this part of study has been made: soot structures become more mature from the initiation to the end. The detailed evolution and transition in terms of soot morphology and nanostructure will be discussed in Chapter 5.

Chapter 3.

Methodology

There are three main parts included in the methodology part. First part is about the optical diesel engine and its setup as a foundation of this study. Second part is about the optical/laser-based imaging diagnostics to observe in-cylinder reactions and soot. The last part is about soot sampling experiments and TEM imaging, which provides information about soot structures.

3.1 Optical diesel engine

The optical/laser-based diagnostics and direct soot sampling method were applied to a single cylinder, automotive-size optical compression ignition engine (Figure. 3.1). The engine specification and operating conditions are listed in Table 3.1. The displacement volume of the engine is 497.5 cm^3 and the bore/stroke are 83 mm and 92 mm, respectively. The combustion chamber is composed of the cylinder head and the cylindrical piston bowl with a compression ratio of 17.7 (geometric). One of the intake ports has a swirl flow passage with a resulting swirl ratio of 1.4. Figure 3.2 shows the simplified schematic of the diesel engine and optical imaging. There are three different types of quartz windows in the engine including a piston window, a bowl rim window and cylinder liner windows. The liner and bowl-rim windows are used to provide the laser beam access while the

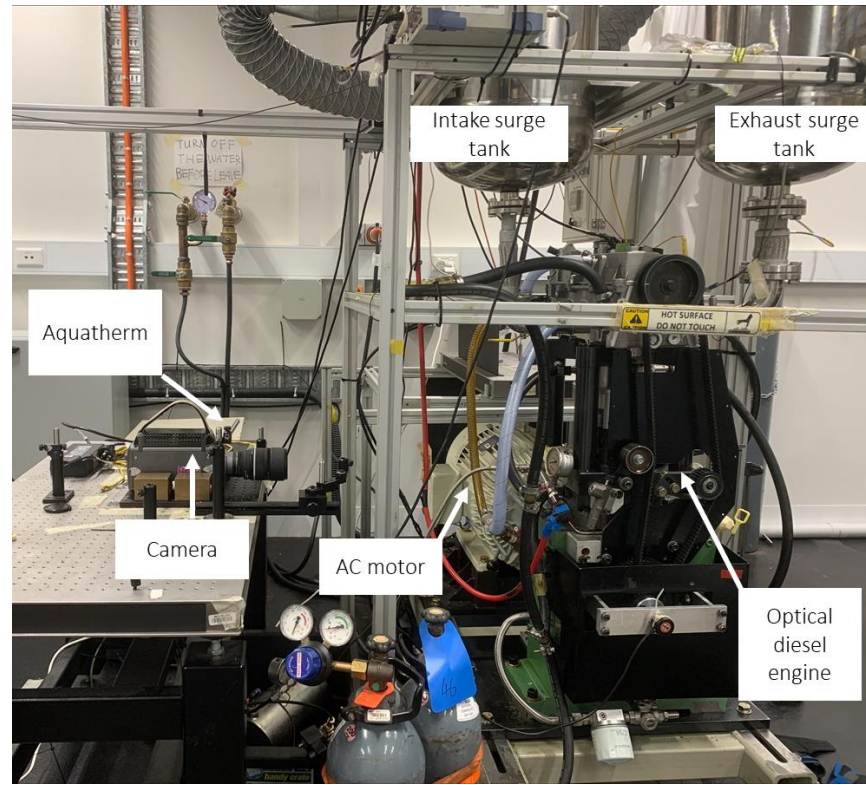


Figure 3.1: Single-cylinder optical diesel engine assembly

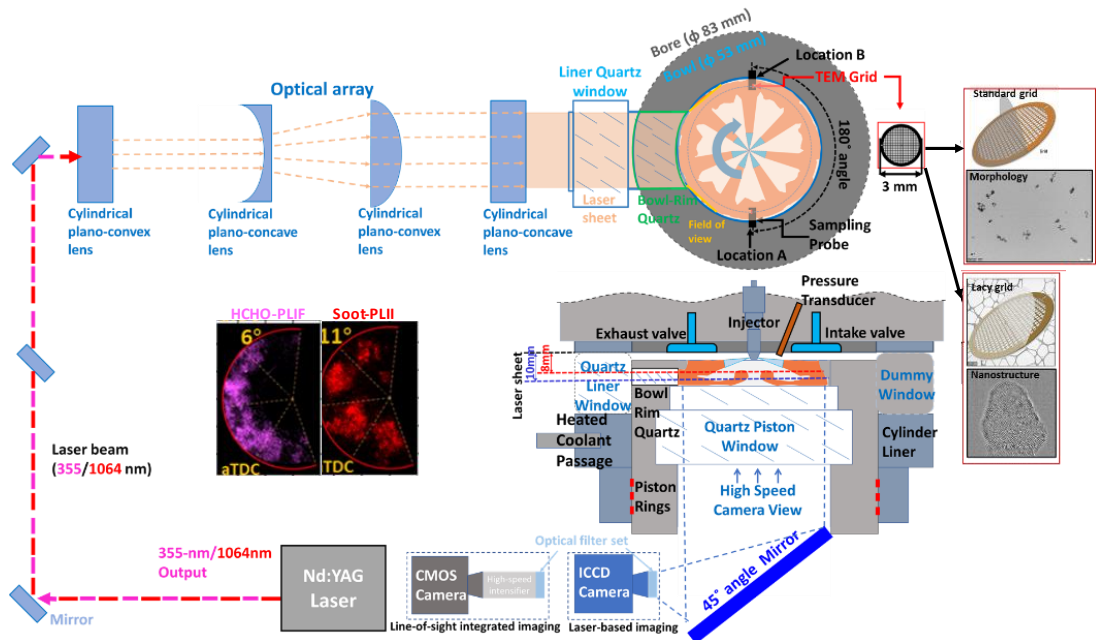


Figure 3.2: Sketch of the optical compression ignition engine, optical/laser-based imaging diagnostics setup and in-flame soot sampling system. Example images of the combined HCHO-PLIF and the soot-PLII signals are presented in the middle. The soot probes installed at location A and B and two different types of standard and lacy transmission electron microscope (TEM) grids used for soot structure analysis are shown on the top-right corner

Table 3.1 Engine specification and operating conditions

Displacement (single-cylinder)	497.5 cm ³
Bore/Stroke	83/92 mm
Compression ratio	17.7:1 (Geometric)
Swirl ratio	1.4
Injection system	Common-rail injector (Bosch CP3)
Fuel	AR04, AR14, AR24 and conventional diesel
Nominal nozzle hole diameter	134 μ m
Nozzle hole type	Hydro-grounded, K1.5/0.86
Nozzle hole included angle	150°
Engine speed	1200 rpm
Coolant temperature	363K
Intake air temperature	303K
Firing mode	10-skip firing

and a 45° mirror. This optical path is shown in the side-view image in Figure 3.2. To achieve planar laser imaging, a 300 μ m thick laser sheet was made from an original circular beam using a series of sheet-making optics. This laser sheet is slightly diverged due to the cylinder liner window and bowl-rim window, which covers the almost all piston bowl region. The beam coverage was effective with no dead zone as previously shown in both the mock- up test and the same optical engine [78,79]. A common-rail injector (Bosch) with seven 134 μ m holes (nominal diameter) was used for fuel injection. The included/umbrella angle of the injector nozzle tip is 150°. Three surrogate jet fuels with 4%, 14% and 24% aromatics (AR04, AR14 and AR24) were tested in the present study. The selected operating conditions are summarised in Table 3.1. Due to the significant impact of ambient gas conditions on soot formation [80–82], the coolant temperature was fixed at 363 K using a water heater/circulation (Thermalcare Aquatherm). The heated engine head, cylinder liner and engine block resulted in thermally stable conditions, setting the same ambient gas pressure/temperature at the time of fuel injection. The fuel injection was executed every tenth motoring cycle (*i.e.* 1 firing and 9 motoring cycles) to

keep the thermal stress below the quartz windows limit and to fully remove residual gases from the previous fired cycle, which also create an undisturbed environment for soot evolution. It is worth noting that the exhaust gas recirculation (EGR) was not applied in the experiment while the intake air flow rate was fixed. Therefore, this 10-skip-firing mode will not alternate the in-cylinder oxygen concentration and following soot formation process. This injection control was performed using a universal timing control unit (Zenobalti 9013-P). Using a pressure transducer (Kistler 6056A), the in-cylinder pressure was recorded, with which the apparent heat release rate was calculated during the optical/laser-based imaging and soot sampling experiments. Given optical/laser diagnostics and soot sampling experiments were performed one at a time, the in-cylinder pressure traces of all fired cycles were compared, and only the images obtained within small cyclic variations in pressure traces were selected for image processing. As to be shown in the results and discussion section, cyclic variations are unavoidable and they are clearly shown in the measured in-cylinder pressures. The pressure traces for all firing cycles were recorded, and the ensemble averaged traces for each run are presented in the results. All the individual runs exhibit very similar combustion phasing and profile. Notably, the skip-firing strategy does not impact the cyclic variation level as shown in the measured pressure traces with only minor variation range.

3.2 Fuel properties

The properties of the three custom-made jet fuels are shown in Table 3.2. They were made and tested by DEVCOM Army Research Laboratory following the ASTM standards. To each fuel property, the standard test method used in this study is noted including the total aromatics (ASTM D1319). The fuels were formulated based on kerosene with cetane number of 40 [83]. To achieve a variation in aromatics between 4 vol% and 24 vol%, the saturates were substituted with aromatics and olefins, meaning that higher aromatic fuels contain lower saturates but higher carbon content. The exact compositions were determined to achieve a systematic variation of aromatics with a very low level of variations in viscosity, density, flash/ boiling point, cetane number and calorific (lower heating) value among the three fuels. This was successful as shown in Table 3.2, suggesting the aromatic variation in the present study is isolated from these important

Table 3.2 Fuel chemical composition and physical properties

Fuels	AR04	AR14	AR24	Diesel
Aromatics [vol.%]	4.3	13.7	24	24
Olefins [vol.%]	0.6	0.8	0.4	-
Saturates [vol.%]	95.1	85.5	75.6	-
Carbon content [wt.%]	85.4	85.1	86.4	
Hydrogen content [wt.%]	14.7	14.2	13.6	
Kinematic viscosity [mm ² /s]	3.9	3.18	2.86	
Density [kg/m ³]	776	783	798	848
Flash point [°C]	42	42	40	38
Boiling point [°C]	258	250	259	180~360
Cetane number	40	41	40	51
Lower heating value [MJ/kg]	43.82	43.76	43.01	44

fuel physical properties. As a reference properties of a conventional diesel fuel is also shown in the table.

3.3 High-speed imaging

Three different high-speed imaging diagnostics were performed in the present study including chemiluminescence imaging of cool flame signals and electronically excited hydroxyl (OH^*) signals as well as natural combustion (soot) luminosity [84]. Among them, the cool flame is a good indicator of low-temperature reaction (HCHO), and the OH^* signal is the indicator of high-temperature reaction. The signal intensity could reflect the strength of the reactions, and the distributions exhibit the in-bowl location of reaction zones. They were conducted using the same high-speed CMOS camera (VisionResearch Phantom v7.3) as illustrated in Figure 3.2 with different optical filters and with or without a high-speed image intensifier (InvisibleVisible UVi-2550B). Given the cool flame

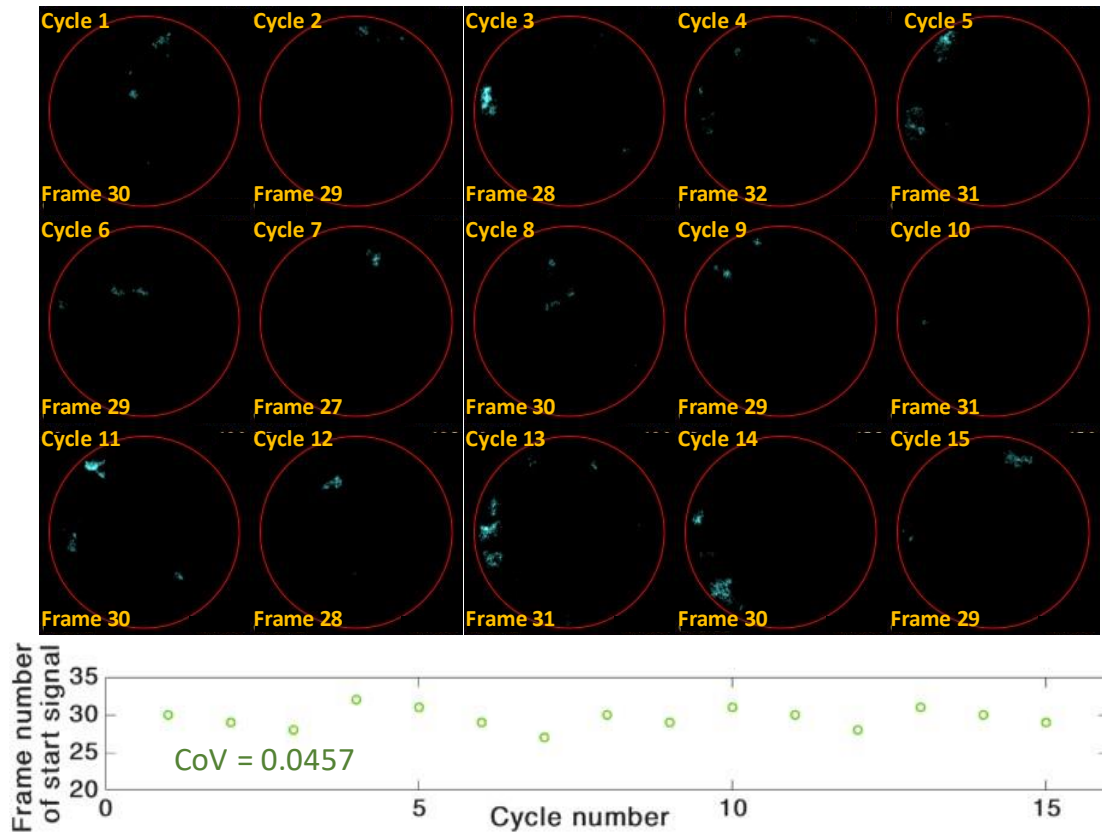


Figure 3.3: The first signal frame of OH^* chemiluminescence images from 15 cycles for AR14 fuel. The bottom plot shows the variation level of the start timing of OH^* chemiluminescence signal

chemiluminescence signals emitted in the 360 ~ 560 nm range [85,86] are very weak and no interference signals are present, no optical filters were used and the intensifier gain was set at 70%. The frame rate used for high-speed imaging was 14,440 frames/s (0.5 °CA/ frame at 1200 rpm) with exposure time of 67 μ s. For the imaging of high-temperature reaction development, 310 nm ultraviolet emission (*i.e.* OH* chemiluminescence) [21,78,87,88] was recorded using optical filters comprising a long pass (WG-305 glass) filter and a band-pass filter centred at 300 nm with 40 nm FWHM. The intensifier gain setting was reduced to 50% due to higher signal intensity than the cool flame chemiluminescence. In addition, high-speed imaging of soot luminosity signals was performed to understand the overall sooting level and the temporal flame development of each fuel [89,90]. Similar with our previous work [43,44], the unfiltered combustion luminosity signals are dominated by soot, which were captured using the same high-speed camera as of the chemiluminescence imaging but without intensifier. As a result, the higher frame rate and shorter exposure time of 36,000 frames/s (0.2 °CA/frame at 1200 rpm) and 3 μ s were used.

Figure 3.3 shows OH* chemiluminescence images at the time of first detectable signals. An example is shown for AR14 fuel to discuss cyclic variations. The images indicate the OH* chemiluminescence emerges from various locations within the piston bowl and the timing can vary between frame 28 and 31 (*i.e.* 3 frames or 1.5 °CA). The calculated coefficient of variation (CoV) is 0.0457 for the selected case. Considering these cyclic variations, the CoV was calculated for the high-speed OH* chemiluminescence movies of all three fuels and discussed together with the signal intensity and distribution in the following section.

3.4 Planer laser induced fluorescence/incandescence and the image selection method

Three types of planar laser imaging was performed for each of the three jet fuels using an Nd:YAG laser (SpectraPhysics Pro-230, 10 Hz) to provide a desired wavelength for excitation or pumping of the dye laser (Rhodamine-6G filled Sirah CobraStretch). The planar laser induced fluorescence imaging was conducted for formaldehyde (HCHO-PLIF), which is a 355 nm-excited LIF signal, to show the development of low temperature

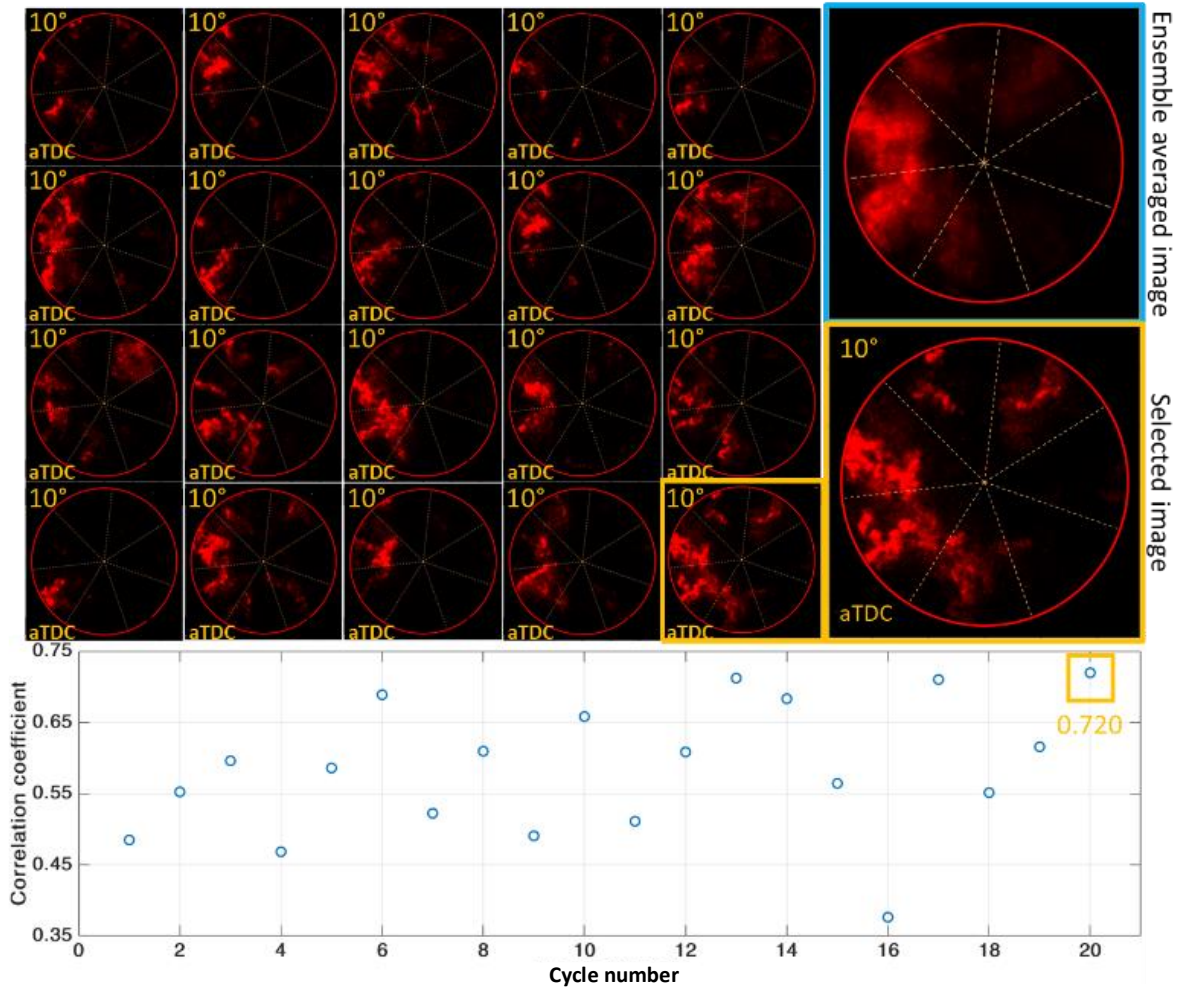


Figure 3.4: Individual soot-PLII images from 20 cycles for AR24 at 10mm laser plane as an example (10°CA aTDC), the ensemble averaged image of 20 cycles (blue frame), and the selected image (yellow frame). The cross-correlation coefficients are plotted at bottom, and the selected image has the highest coefficient (0.720) as marked with yellow box

reaction [79]. For this, the Nd:YAG laser was set for 355 nm with 160 mJ/pulse, which returns emissions in the range of 380 ~ 450 nm [91]. The signal was isolated using a 385 nm long-pass filter, a 430 nm band-pass filter (10 nm FWHM) as well as a 450 nm short-pass filter to remove the interference from laser induced soot incandescence and other species [91]. The final filtered signals were later recorded by an ICCD camera (LaVision Nanostar) [92]. For planer laser induced incandescence (soot-PLII) imaging, a 1064 nm laser beam from the Nd: YAG laser with 200 mJ/pulse was used to cause incandescence signals. This exceeds the soot sublimation energy and thus is enough to expect a linear correlation between LII signal intensity and soot volume fraction [93]. The same ICCD camera was used to record the LII signals in the shorter wavelength range with a short-pass filter (450 nm) and a band- pass filter (430 nm).

The imaging was repeated for three custom-made fuels with aromatic variations. For each fuel, the laser sheet height was varied between 8 mm and 10 mm below the fire deck (flat cylinder head) to understand the flame motion in the r-z plane. For the presentation of PLIF/PLII images, an individual cycle selection approach was used as our previous study [93]. From a set of 20 images taken for 20 firing cycles, a representative image was selected. This selection was conducted systematically through calculation of cross-correlation coefficients, which returns one individual cycle image with the highest similarity to the ensemble-averaged image from the pixel-by-pixel comparison. This approach was proven effective as the turbulent HCHO and soot structures are maintained, which are lost in the ensemble-average images due to the smearing-out effect.

The laser-induced signal images were acquired for various crank angles to discuss a temporal development of HCHO and soot (PLII) distributions, similar with previous studies [91,94]. For each crank angle, 20 engine cycles were imaged, which exhibits inherent cyclic variations. An example is shown in Figure 3.4 for 20 PLII images taken

at 10 crank angle degrees after the top dead centre (10 °CA aTDC) and at 10 mm laser plane below the cylinder head. The example is shown for AR24 fuel. Due to very high sooting condition of this fuel, the beam attenuation issue is significant on the right side of the piston bowl window. The signals are clearer on the left side but the cyclic variations in the spatial distribution of LII signals are significant. When these individual cycle images are averaged, there is a smearing-out effect that could lose the turbulent signal distributions [94]. Therefore, an alternative method was used to select an individual cycle for presentation based on the pixel-by-pixel calculation of cross-correlation coefficients. This returns an individual cycle image that resembles the ensemble averaged image the most while preserving the complex signal distributions.

3.5 Multi-location in-flame soot sampling

For morphology and internal structure analysis of soot particles, a thermophoresis-based, direct soot sampling method was applied as in the previous studies [8,9,44,45]. In order to make sure the soot process during soot sampling experiments is as of the imaging experiment, the sampling was performed in the same optical diesel engine. The sampling probes were positioned at 10 mm below the cylinder head, which was consistent with the lower soot-PLII plane. The sampling probes were mounted on the piston bowl wall using a small set screw to hold two types of TEM grids at the probe tip one at a time: a 400-mesh, 3 mm diameter copper grid with carbon coating (CF400-Cu) and a 300-mesh lacy grid (LC300-Cu) for soot aggregate/primary particle morphology analysis and sub-nano scale internal structure analysis, respectively. These grids are positioned in a small groove made on the probe body and protected from the excessive heat of the flame using a cover plate. To expose the grids to hot soot particles within the flame, a 2-mm diameter hole was drilled on the probe tip. The restrictive passage protected the carbon layers from the damages caused by excessive heat. The thermophoretic force is high between the hot soot

and the cold TEM grid and thus the particles are deposited on the grid surface while immediate reaction quenching occurs to freeze the soot reaction. The optical engine operation procedure for soot sampling was as of the previous studies successfully reporting soot structure variations due to fuel injection pressure, swirl effect, fuel jets interactions and fuel aromaticity [43,44,46,74,95]. This includes motoring for 90 seconds before firing and the selected number of fuel injections onto the sampling probes, which ensured enough number of soot aggregates sampled for statistically meaningful data analysis while avoiding the bias associated with soot overloading. After the fuel injection cycles, the engine motoring stops, the cylinder liner is dropped down and the soot sampling grids are collected. Once the recorded pressure traces are confirmed to be consistent with previous engine runs, and the sampled soot particles are checked. The same procedure was repeated until the soot sampling was successful for each fuel.

3.6 TEM imaging and post-processing

The sampled soot particles were imaged using a standard TEM (JEOL 1400) with 30,000 and 100,000 magnifications. The accelerating voltage was set at 120 kV and the recording CCD camera resolution was 4100 pixel by 3000 pixel. Some examples of standard TEM images (x100,000 magnification) are shown on Figure 3.5. A few soot aggregates are seen exhibiting significant variations in size and structure. A total of 30 and 10 TEM images were recorded from varied on-grid locations under 100,000 and 30,000 magnification settings. The soot aggregates and primary particles within the aggregates were analysed using a post processing code written on Matlab [95–97] – example images are shown in Figure 3.6. However, for a given sampling location, the image-to-image variations are very high, which raises an uncertainty concern [98]. This variation required a large sample size – over 27 TEM images in the example case to ensure the differences

shown in the soot aggregate size (radius of gyration) and the primary particle size (mean diameter) are real.

With a high-resolution TEM (Philips CM200), the sub-nano scale analysis of carbon-layer fringes was performed. The accelerating voltage and point resolution of this high-resolution TEM were 120 kV and 0.25 nm. The images were recorded with a 470,000 magnification setting and the CCD camera resolution of 2048 by 2048 pixels. For each sample, a total of 10 HR-TEM images were taken. An example image is shown in Figure. 3.6. Differentiated from the flat background, the soot particle regions show a rough texture due to the cross-cut view of carbon-layer fringes. The post-processing of the HR-

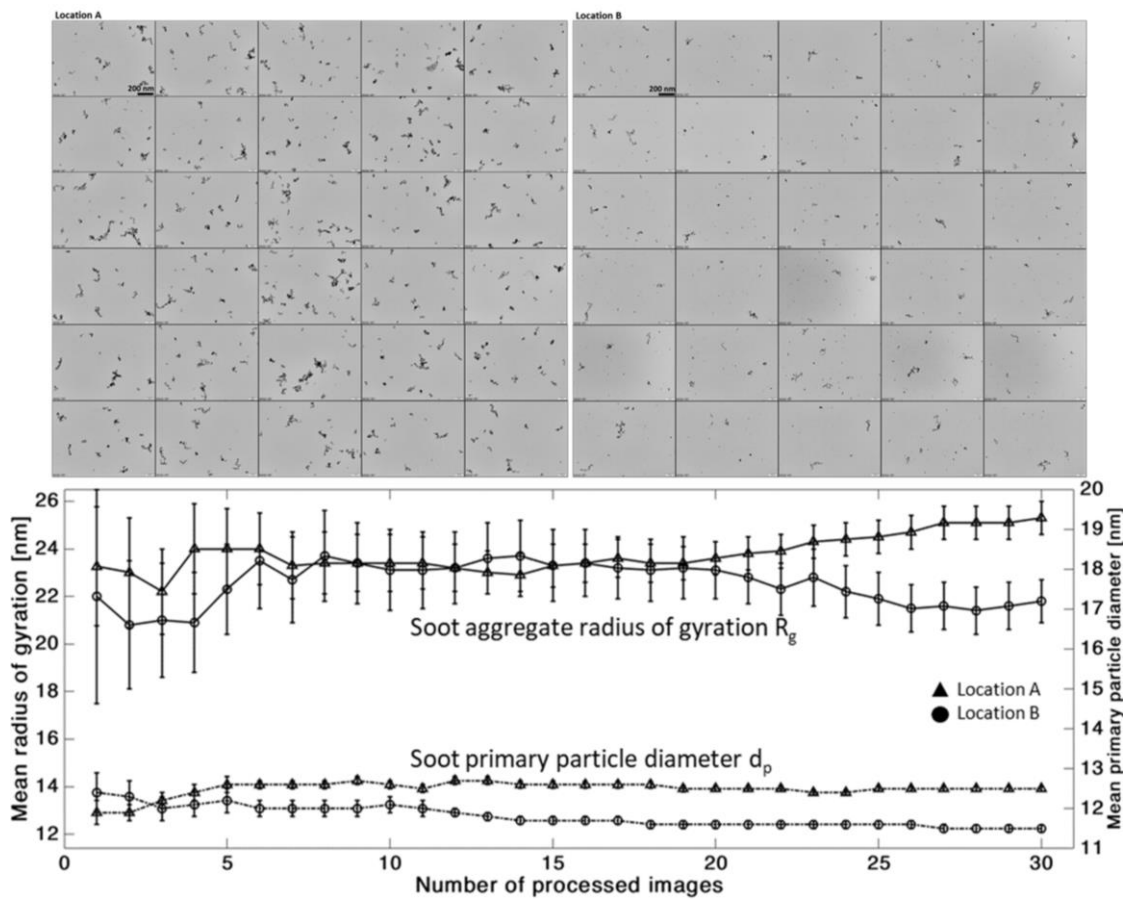


Figure 3.5: Standard TEM images taken at 30 different on-grid locations for the soot samples at location A and location B (top), and the variation of soot aggregate radius of gyration and primary particle diameter with increasing number of processed TEM images (bottom) for the location A and location B. The results are presented for AR24 fuel

TEM image was also performed to extract carbon-layer fringes [75], which are displayed as black lines in Figure. 3.6. This process is automated with an in-house developed Matlab code [44]. Since variations in these statistics depend on the imaged soot particles or part of the soot particles, a total of 10 HR-TEM images were obtained. In Figure 3.7, it is shown that the measured mean fringe length and tortuosity statistics converge only when more than 9 HR-TEM are processed. The trends observed from location A and location B samples will be discussed later with the results of all three jet fuels. Figure 3.6 also shows an example image for the concentricity map of a selected soot primary particle. The extracted fringes were further analysed for concentricity [36], which shows the distribution and orientation of carbon-layer fringes within the soot primary particles. This effectively determines the core and the outer shell region of the soot primary particle with lower concentricity values (*e.g.* 0.3~0.35) indicating a disordered amorphous core structure and higher values (*e.g.* 0.55~0.6) meaning ordered carbon-layer fringes forming a centred shell structure.

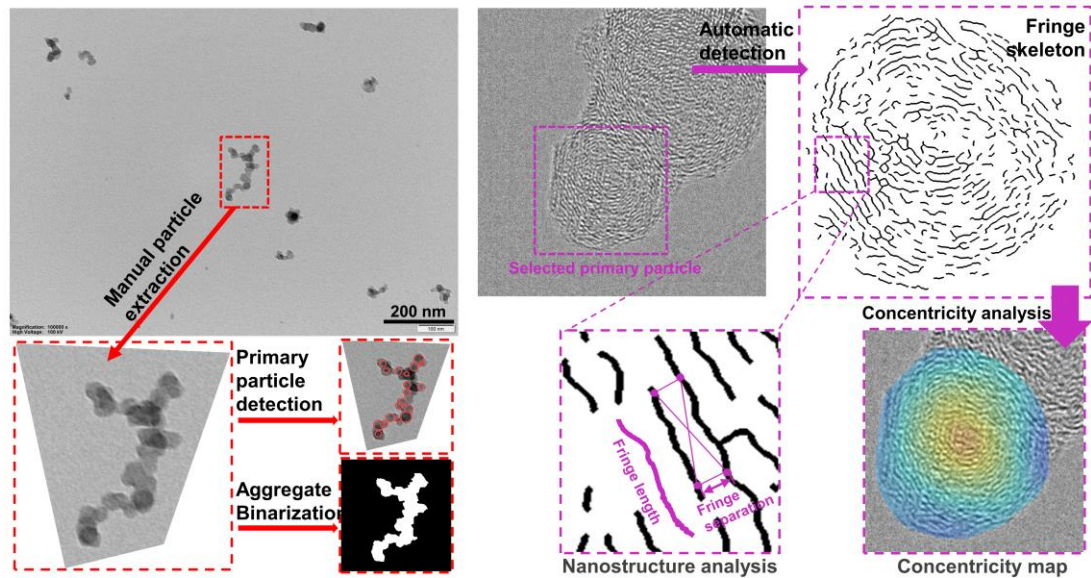


Figure 3.6: Soot particles morphology and internal structure analysis

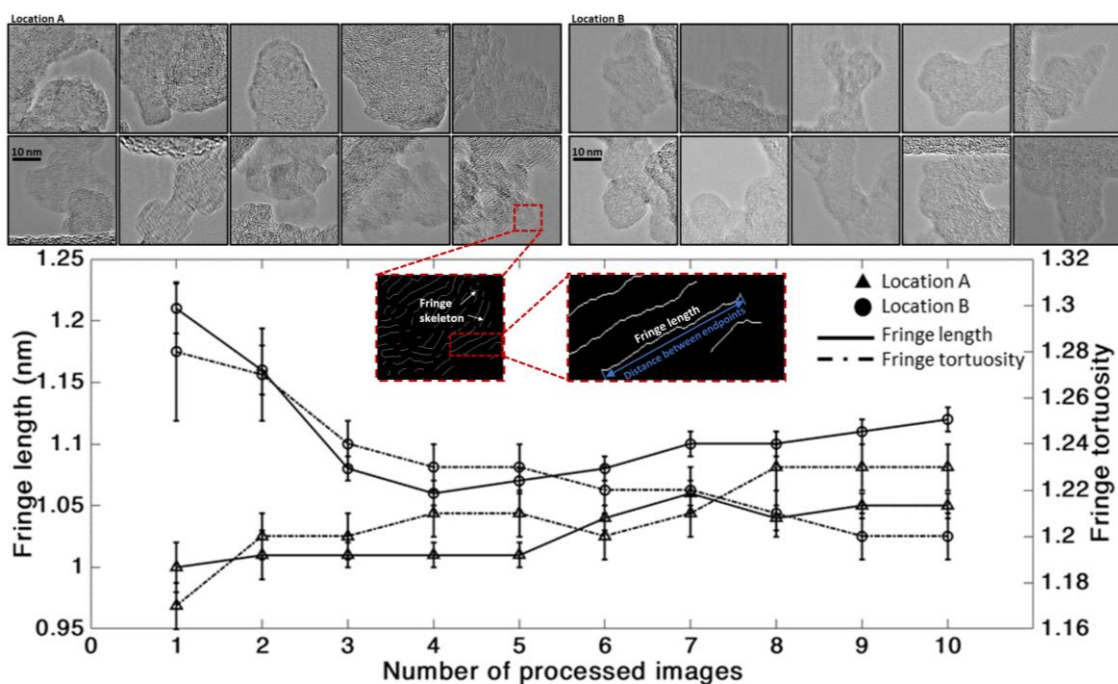


Figure 3.7: High resolution TEM (HR-TEM) images taken at 10 different on-grid locations for the soot samples at location A and location B (top), and the variation of soot primary particles fringe length and fringe tortuosity with an increase in processed HR-TEM images (bottom) for the location A and location B. The results are presented for AR24 fuel

Chapter 4.

Aromatics effect on in-flame soot distribution and morphology

The influence of fuel aromatics on combustion and soot structures is studied using three custom-made surrogate fuels with 4%, 14% and 24% aromatic content as shown in Table 4.1. The injected fuel mass is fixed, which is delivered at 50 MPa using a conventional 7-hole injector. This creates an in-cylinder environment similar with the real running engines. The air to fuel ratio is also almost identical for all three fuels due to the fixed

Table 4.1 Engine operating conditions for varying aromatic fuel study

Number of holes	7
Fuel	AR04, AR14 and AR24
Injection pressure	50 MPa
Pilot injection mass and timing	1.8 mg and 11 °CA bTDC
Main injection mass and timing	7.2 mg and 5 °CA bTDC
Engine speed	1200 rpm
Indicated mean effective pressure	377 ~ 392 kPa

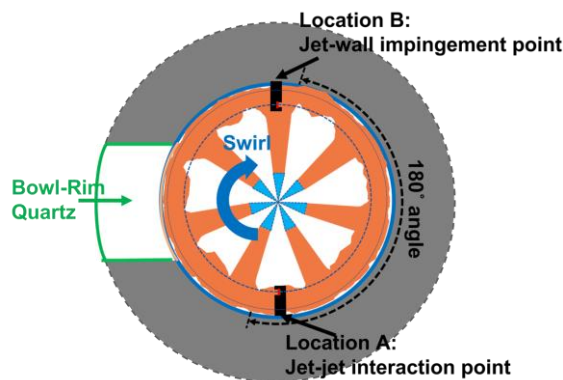


Figure 4.1 Illustration of in-bowl soot sampling locations used for the aromatics effects study

intake air mass flow rate and almost identical C-H ratio. A typical pilot-main injection strategy is implemented with the pilot injection at 11 crank angles before top dead centre ($^{\circ}\text{CA}$ bTDC) and the main injection at 5°CA bTDC. These are selected to achieve the fixed combustion phasing, which can affect the combustion and soot formation significantly. For thermophoretic soot particle sampling, two in-bowl soot sampling locations are investigated including the jet-jet interaction region (location A) and jet-wall impingement region (location B) as illustrated in Figure 4.1.

4.1 Pressure traces, heat release rate and high-speed images

The in-cylinder pressure recorded during the optical/laser-based imaging and soot sampling experiments of the current study is shown in Figure 4.2 (top). The colour

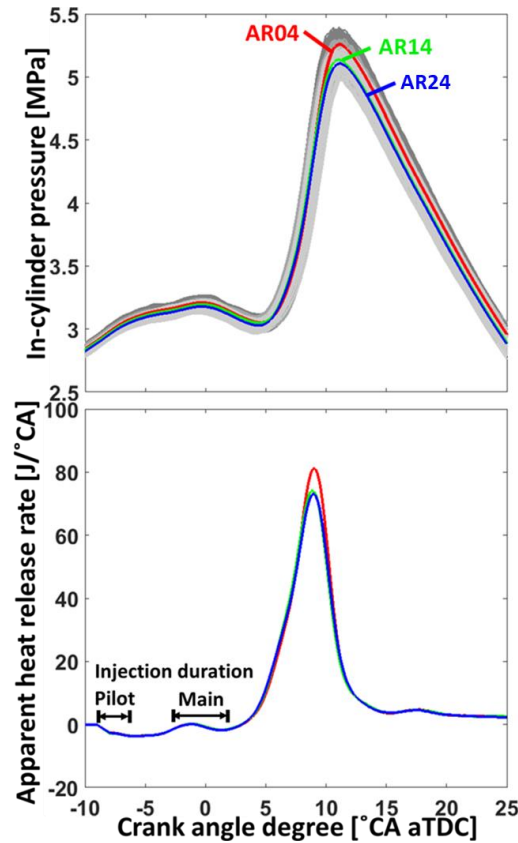


Figure 4.2: In-cylinder pressure traces of all measured individual cycles and their ensemble average (top) and the calculated apparent heat release rate (aHRR) traces for AR04, AR14 and AR24 fuels. The duration of pilot and main injections is illustrated on the aHRR traces

scheme, as red, green and blue, represents the ensemble-averaged pressure traces for AR04, AR14 and AR24 fuel. In addition, the grey lines with varying brightness are plotted using the individual pressure traces measured for more than three hundred individual cycles for each fuel. The in-cylinder pressure plot indicates the optical diagnostics performed in this study were under very similar in-cylinder pressure conditions. In other words, the differences seen for fuel variations are within the cyclic variation range, thanks to the similar physical properties of the formulated fuels. The calculated apparent heat release rate traces (aHRR) are also plotted at the bottom of Figure 4.2 (bottom) with the illustration of actual injection timing and duration for both pilot and main injection events. From the aHRR traces, it is clear that the combustion phasing was matched well, once again suggesting similar in-cylinder gas conditions for the optical/laser-based imaging and soot sampling diagnostics. Moreover, the fuel injection-induced evaporative cooling and the magnitude of heat release during the low-temperature reaction and late-stage decline are almost identical, indicating very similar fuel vaporisation, first-stage ignition as well as late-cycle burn-out processes.

To evaluate the low- and high-temperature reaction trends, some selected cool-flame and OH* chemiluminescence images are shown in Figure 4.3. The signals are from HCHO and OH radicals during the reactions. False colouring was used to differentiate cool flame signals (orange) and OH* chemiluminescence signals (cyan). All the high-speed images were processed in an identical set of parameters, and thus the signal intensity could show a relative difference in the corresponding reaction strengths. For instance, in the case of cool flame images, higher cool flame signal intensity indicates higher amount of HCHO at the specific crank angle timing, whereas the decreasing signal indicates the consumption of HCHO. The location of the signal exhibits where the HCHO was concentrated within the piston bowl. For ease of interpretation, seven jet axes and piston

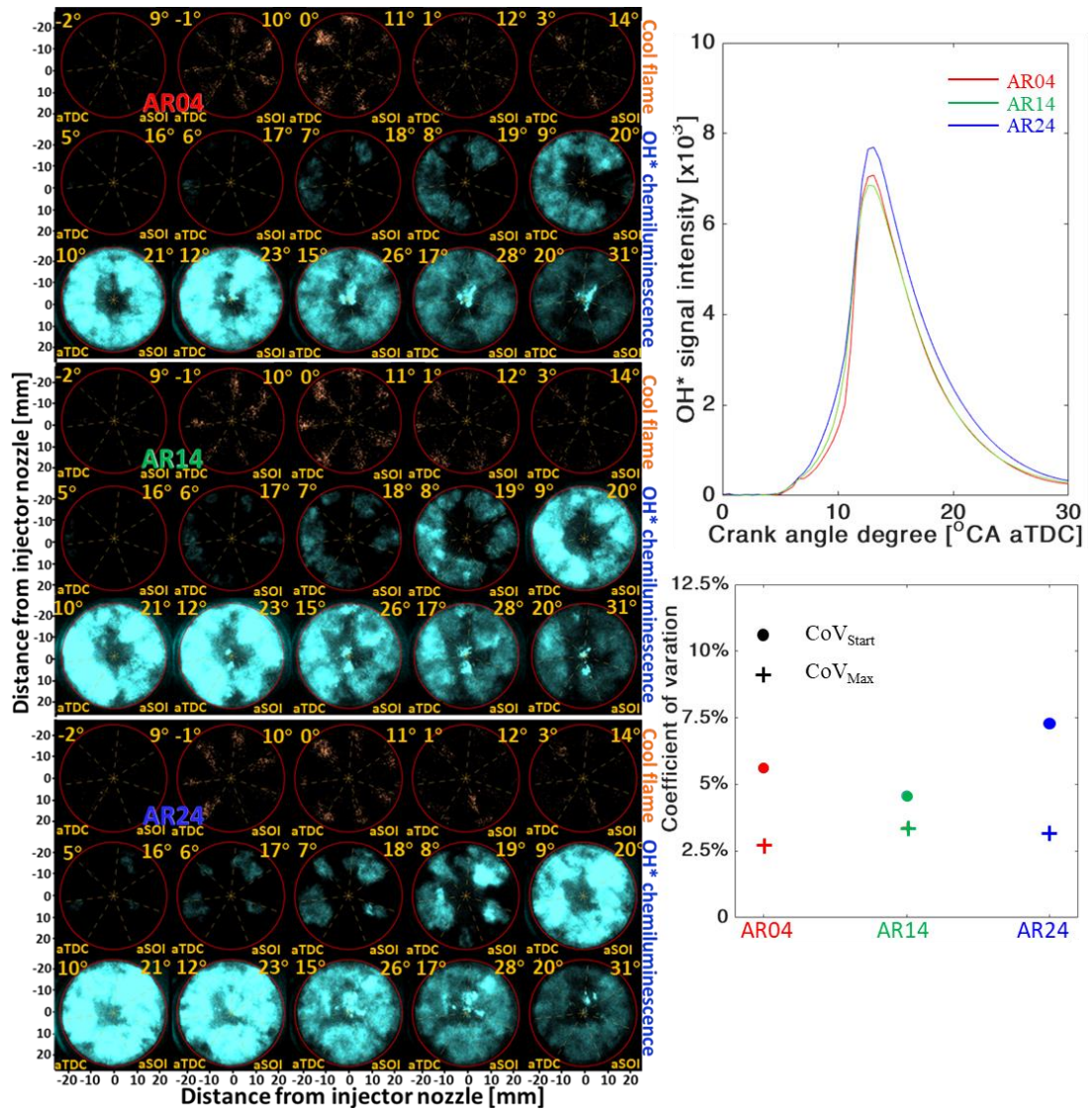


Figure 4.3: Cool flame chemiluminescence and OH* chemiluminescence images of a selected cycle for AR04, AR14 and AR24 fuels. Shown at the right are the OH* signal intensity profiles and the CoVs of the first detected OH* chemiluminescence timing and the maximum timing

bowl wall are illustrated with orange dash lines and a red solid line. The crank angle timing is annotated at the top-left corner while the time after the end of injection (aEOI) is shown at the top-right corner of each image. Furthermore, the average intensity profiles of OH* chemiluminescence signals are plotted for all three AR fuels (top-right) together with the CoV of the first OH* chemiluminescence timing (CoV_{Start}) and the maximum signal intensity (CoV_{Max}).

Figure 4.3 indicates that the overall development pattern of the flames is very similar regardless of fuel aromatics. The cool-flame signals first appear as multiple pockets around the jet axes at 2 crank angles before top dead centre ($^{\circ}\text{CA}$ bTDC). Those signals grow rapidly in both intensity and coverage near the bowl wall as the low-temperature reaction continues.

For all three fuels, the first OH^* chemiluminescence signals emerge at approximately 5°CA after TDC (aTDC). The OH^* chemiluminescence increases and reaches the peak at about 12°CA aTDC regardless of the fuel type. The estimated CoVs of the first OH^* signal timing and maximum signal timing are $4.5 \sim 7.3\%$ and $2.7 \sim 3.4\%$, respectively. Regarding the spatial distribution, the OH^* signals are first detected near the wall, where the strong cool-flame signals developed in earlier crank angles. The timing is consistent with the initial increase of aHRR (Figure 4.2), indicating the high-temperature reaction-driven, early-stage combustion. The high-temperature reaction continues with growing OH^* chemiluminescence signals in both the intensity and coverage until the peak signal intensity/coverage is consistently found at around $10 \sim 12^{\circ}\text{CA}$ aTDC in the intensity plot regardless of fuel type, which is also in line with the timing of peak aHRR and in-cylinder pressure. Moreover, the signal coverage and intensity at the peak OH^* chemiluminescence timing is observed almost identical for AR04 and AR14 but is measured higher for AR24 fuel. Increased adiabatic flame temperature associated with higher ring-structured hydrocarbons in fuel was previously reported [51], which might explain the higher OH^* chemiluminescence signal observed. However, it is noted the aHRR did not show an increasing trend for a higher aromatic fuel. It was likely some signal interference from soot luminosity, which caused increased coverage in the line-of-sight integrated signals. After reaching this peak intensity, the OH^* chemiluminescence signals gradually decrease until 20°CA aTDC for any studied fuel of the present study.

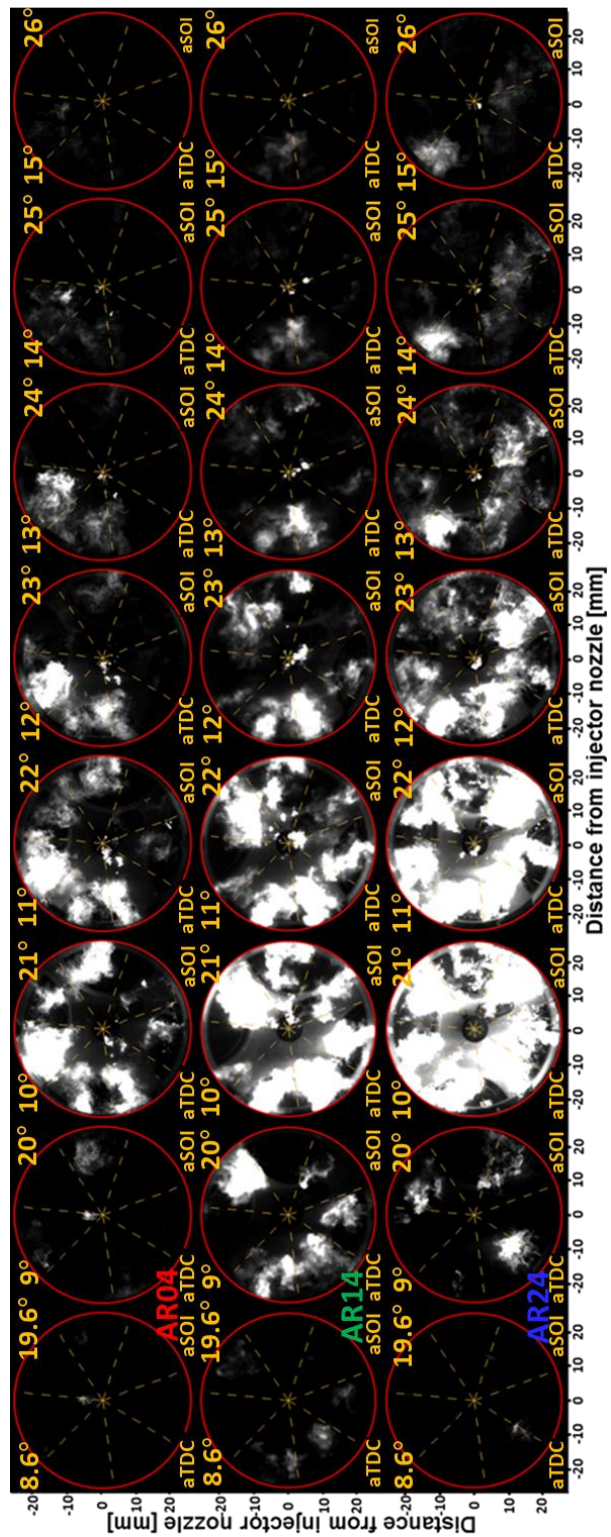


Figure 4.4: High-speed soot luminosity images of a selected cycle for AR04, AR14

Figure 4.4 shows the high-speed soot luminosity images. The presentation format is identical to Figure 4.3. The overall sooting flame development pattern is similar among the three aromatic fuels. At 8.6 °CA aTDC, the weak luminosity signals are scattered as

small pockets in multiple locations of the combustion chamber. These signals become larger with increasing intensity firstly between the jet axes, a region of locally rich mixtures [99,100]. The luminosity signals then expand to form large soot clouds and reach the peak coverage and intensity at near wall regions at 10 °CA aTDC, which is coincident with the timing of peak aHRR and peak OH* chemiluminescence. As mentioned previously, this raised a concern of potential signal interference to the OH* chemiluminescence. The decrease of the strong luminosity signals is rapid with most of them disappearing by 14 ~ 15 °CA aTDC.

While the overall development pattern is similar, the soot luminosity signals in Figure 4.4 show three distinct trends depending on the aromatic fuel. Firstly, the signal coverage increases faster and reaches a higher peak signal intensity for a higher aromatic fuel, indicating higher sooting propensity and stronger soot formation due to this fuel composition change. Secondly, the luminosity signals are more equally distributed for AR24 compared to AR04 and AR14 showing locally concentrated signals only in some regions. These are expected trends knowing aromatics easily survive through the decomposition process and become available for soot formation [62]. Lastly, the soot luminosity signals survive longer for a higher aromatic fuel. For example, some strong signals are present even at 15 °CA aTDC for AR24 fuel while almost no signal is seen for AR04 fuel.

4.2 Planar laser-based images

For the three aromatic fuels, HCHO-PLIF and soot-PLII images were obtained between -1 °CA aTDC (1°CA bTDC) and 20 °CA aTDC. This is a crank angle range corresponding to the cool-flame chemiluminescence signals, through the OH* chemiluminescence signals, and to the soot luminosity signal growth and decay (Figure

4.3 and 4.4). The planar laser images show the cross-cut view of the flames and thus overcome the limitation of the previously shown line-of-sight integrated images. Figure 4.5

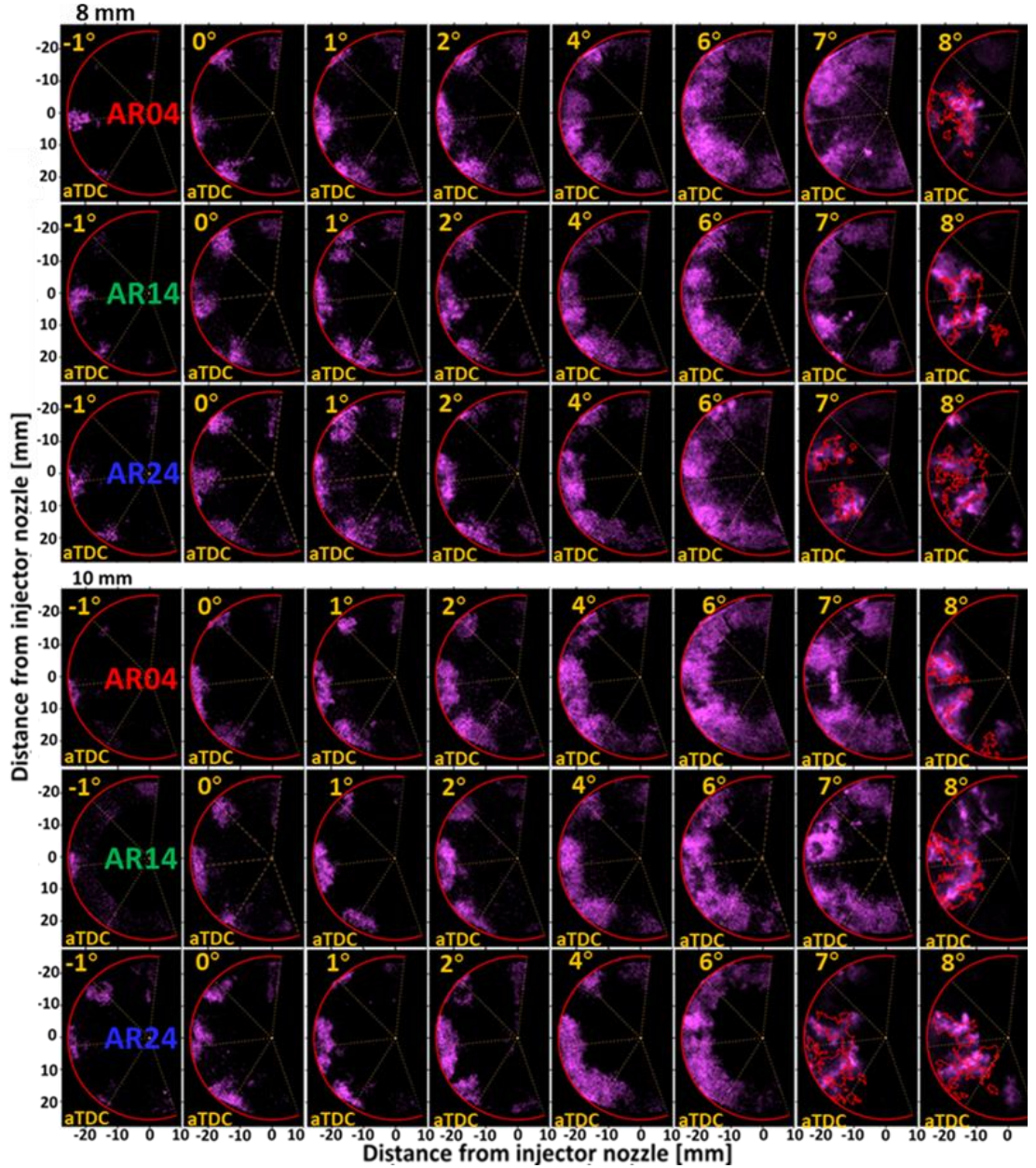


Figure 4.5: HCHO-PLIF images of AR04, AR14 and AR24 fuels during the first-stage ignition phase at 8 mm and 10 mm below the cylinder head

presents HCHO-PLIF images for $-1 \sim 8$ °CA aTDC range at two laser plane heights of 8 mm and 10 mm below the cylinder head. As mentioned in the Methodology section, these

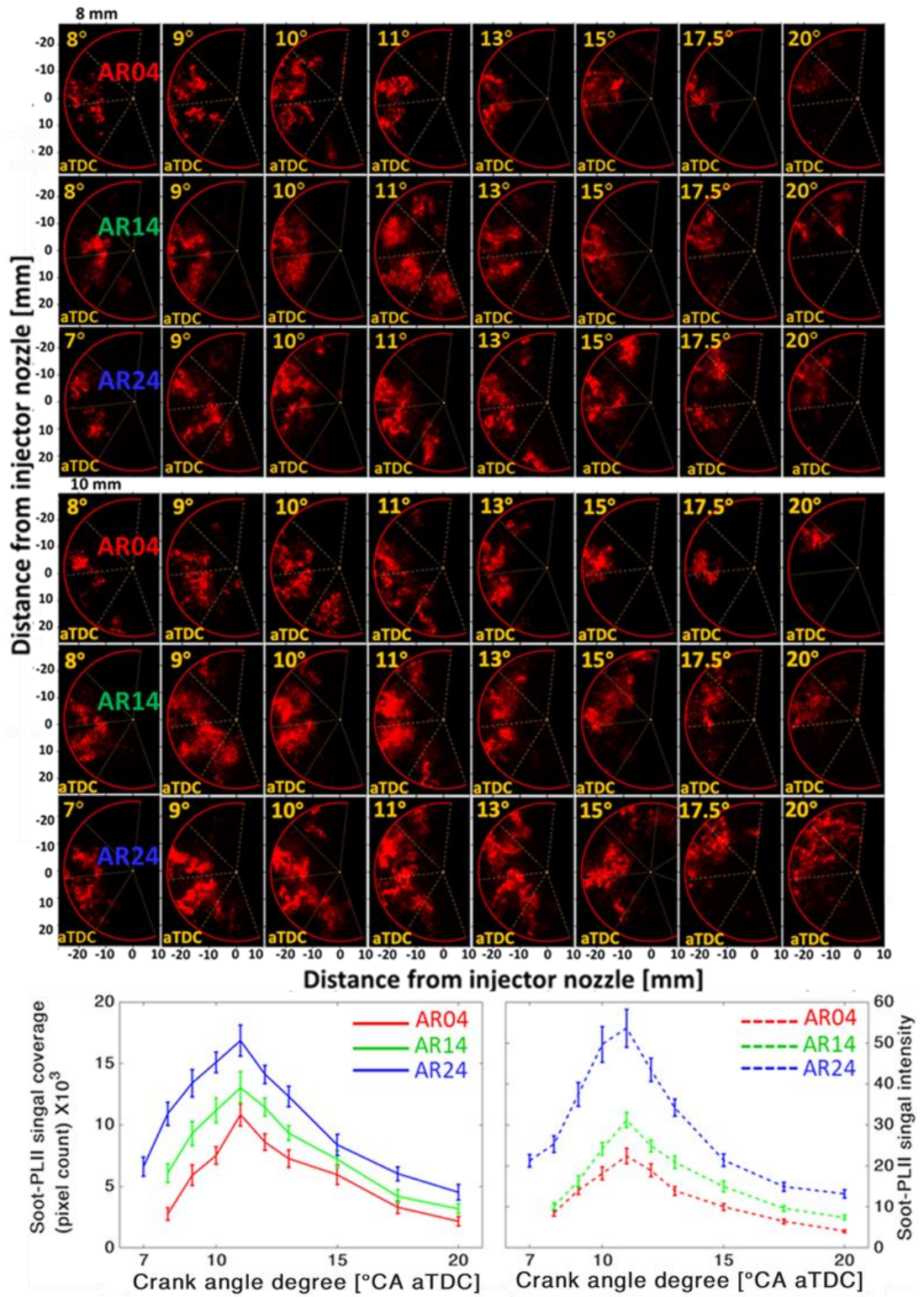


Figure 4.6: Soot-PLII images during the sooting phase of AR04, AR14 and AR24 fuels at 8 mm and 10 mm laser below the cylinder head

are systematically selected images of an individual cycle. It should be noted that the HCHO-PLIF signals shown in Figure 4.5 are potentially affected by other UV excited

signals (e.g. fuel and PAH [101]). This was minimised with the optical filter pack used to isolate the signals, and the HCHO LIF signal development is observed to be very consistent with the aHRR profiles (Figure 4.2) and cool flame signals (Figure 4.3) development. The images are shown for the left-half of the original image due to beam attenuation, which still provide useful information thanks to high similarity of the seven-jet development.

The HCHO signals show a similar distribution for all three aromatic fuels. The HCHO appears in the wall impingement region of each jet. This when it peaks at 6 °CA aTDC for any aromatic fuel. In just one crank angle after the peak timing, the HCHO-PLIF signals disappear from the wall impingement area where the HCHO first emerged. This indicates the consumption of HCHO radicals during the low- to high-temperature reaction transition [79,102]. Concurrently, the HCHO signals turn into fragmented structures and by 8 °CA aTDC, the signals are strong only in the inter-jet region. This distinctively different HCHO-PLIF structure is due to the interference from PAHs [101], which is found to be temporally decoupled from HCHO-PLIF signals. To evaluate this PAH interference, the PLII images were taken at 7 and 8 °CA aTDC. As described with Figure 3.4, a representative individual cycle image was selected for presentation. For later crank angles (7 and 8 °CA aTDC), boundaries of the selected PLII images were overlaid on each corresponding HCHO-PLIF image using red lines. Although the HCHO-PLIF and soot boundaries were acquired from different engine cycles, they overlap and display high similarities in the signal distributions. This suggests the PAH formation and soot inception occurred at 8 °CA aTDC for AR04 and AR14 fuels whereas it occurred earlier at 7 °CA aTDC for AR24 fuel.

For the detailed discussion of soot distributions, the soot-PLII images are presented in Figure 4.6 from 7 or 8 °CA aTDC (*i.e.* the first soot timing) to 20 °CA aTDC. Since the

LII signals have a linear correlation with the soot volume fraction, the PLII signal coverage and intensity are also plotted at the Figure 4.6 bottom. The LII signals are highly concentrated in the jet-jet interaction region for all three fuels, which grow quickly from the first signals to the maximum signals in just 2 ~ 3 °CA. Later, the soot- PLII signals decay while the cloud-like structure transforming into small pockets [8,89]. Regarding the aromatic content in the fuel, a clear trend is shown in the LII signal plots such that a higher aromatic fuel produces more soot to reach a higher peak value in both the coverage and intensity. The signal intensity plot suggests not only the peak soot but the soot growth rate is higher for a higher aromatic fuel. After the peak, the LII signal declines due to soot oxidation. Although the soot oxidation is significant for all three fuels, the soot formation was much higher for a higher aromatic fuel and thus the remaining LII signals at the end of the combustion event (e.g. 20 °CA aTDC) is still higher for a higher aromatic fuel.

4.3 Soot particle structure and statistical analysis

The particle structure level discussion of soot with a variation of fuel aromatic content is presented in Figure 4.7 with some example HR-TEM images, similar with [103]. The images are shown for both sampling location A and B (see Figure 4.7 for the definition). From visual inspection, the carbon layer fringes of the soot particles exhibit a typical core-shell internal structure [104], which is commonly found for all three fuels.

There are multiple amorphous cores observed with many randomly oriented, short carbon fringe segments, indicating that the carbonisation of the soot particles is incomplete [75,104,105]. From Figure 4.7, it is observed that these amorphous cores are composed of short fringes arranged in various orientation. They are surrounded by highly ordered carbon- layer fringes, suggesting more graphitised outer shell structures. From these carbon-layer fringe images, two internal structure parameters were calculated including

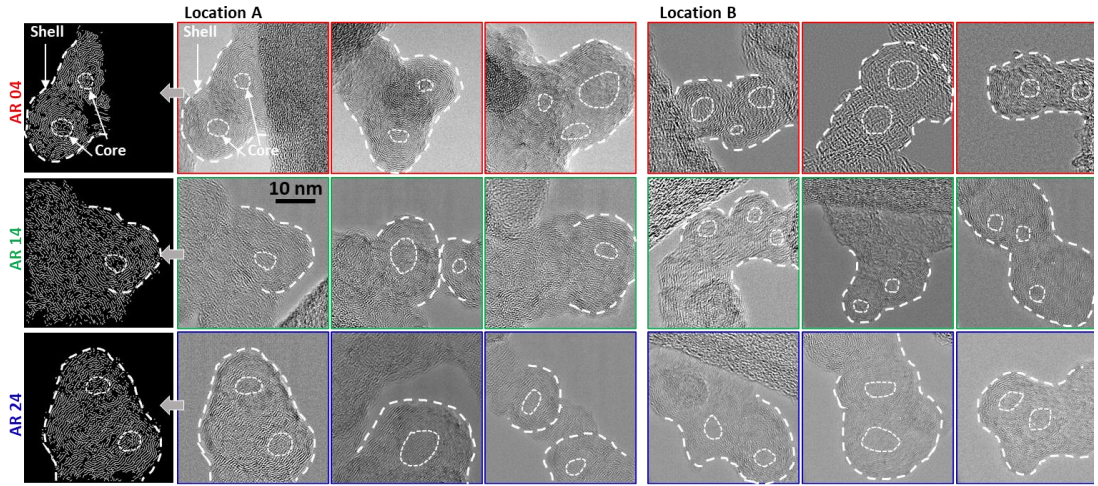


Figure 4.7: High resolution TEM images of soot primary particles sampled at location A and location B for AR04, AR14 and AR24 fuels. The dashed lines and circles illustrate the shell and core regions of the soot primary particles. On the leftmost column, processed carbon-layer fringes are shown using white lines

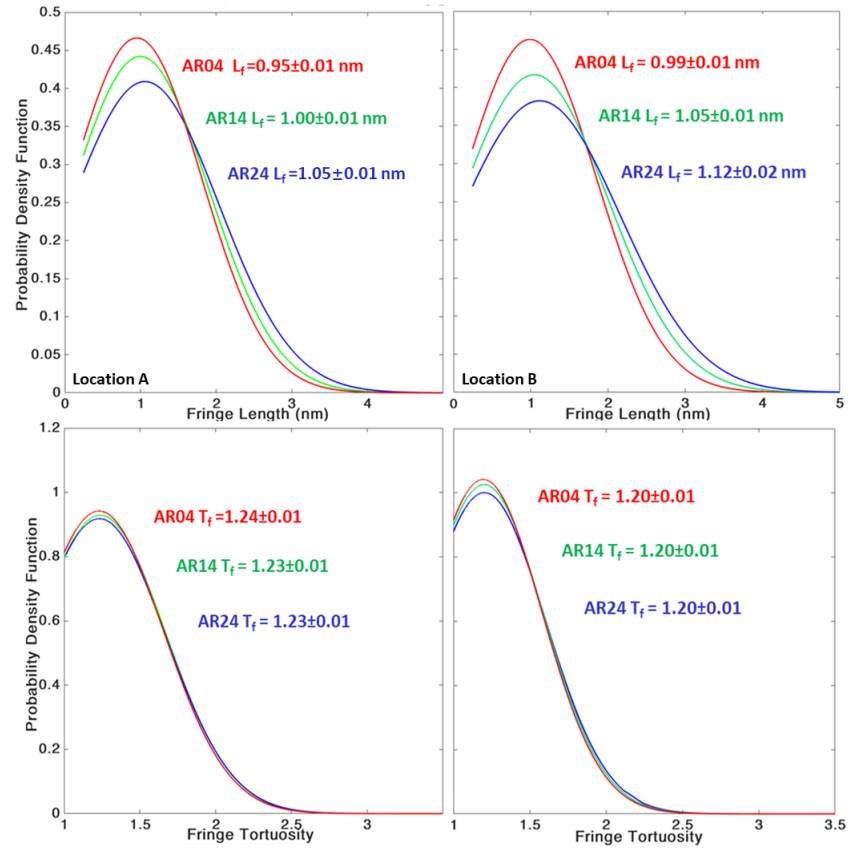


Figure 4.8: Probability density functions of carbon-layer fringe length (top) and fringe tortuosity (bottom) for soot primary particles of AR04, AR14 and AR24 fuels at location A (left) and location B (right) with the 95% confidence error range

the fringe length and fringe tortuosity. The results are shown in Figure 4.8 as probability

density functions (PDFs). On each PDF line, the mean value and error margin of 95% confidence interval are annotated. Figure 4.8 shows that the fringe tortuosity – *i.e.* the level of bending of carbon layers – does not show significant differences due to the amount of aromatics in fuel. However, the fringe length shows a statistically meaningful gap with higher length for a higher aromatic fuel on both sampling locations. This indicates that the higher aromatics promoted the growth of carbon layers as the formation of large PAHs was promoted [63].

Figure 4.9 shows the standard TEM images of soot particles for all three fuels. For each fuel selection, four example images are presented from a total of 30 images for each sample. From visual inspection, the soot particles show aggregate structures with a significant variation in size and shape. Some soot aggregates have a compact cluster structure while others exhibit stretched, long chain structures. For a given fuel, location B samples show much smaller and more compact aggregate shapes, and their number counts are significantly lower than those of location A. This is consistent with strong LII signals observed from the jet-jet interaction region (Figure 4.6). Regarding the aromatic content in fuel, the TEM images indicate increased amounts of soot aggregates for a higher aromatic fuel in both sampling locations. Further analysis of soot aggregates comprising various numbers of primary particles was performed for the standard TEM images and the results are shown in Figure 4.10 as a PDF of soot primary particles diameter (d_p) and aggregate radius of gyration (R_g). The aggregates fractal dimension (D_f) was also estimated, and the results are shown together. The mean values are annotated next to each plot together with error margins of 95% confidence interval. The PDFs and the mean value show only minor changes in d_p with the aromatic content variation in fuel, suggesting that the aromatics do not contribute to the size of soot primary particles. Referring to the fringe length increase measured for a higher aromatic fuel, it is

interpreted that the aromatics impact the growth of carbon layers but do not promote the

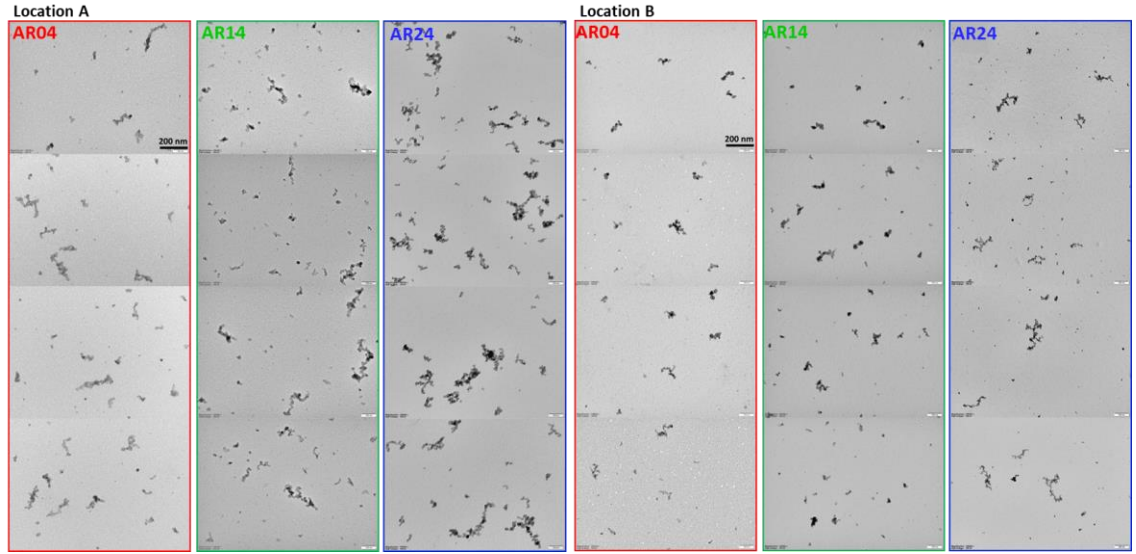


Figure 4.9: The standard TEM images showing soot aggregates sampled at location A and location B for AR04, AR14 and AR24 fuels

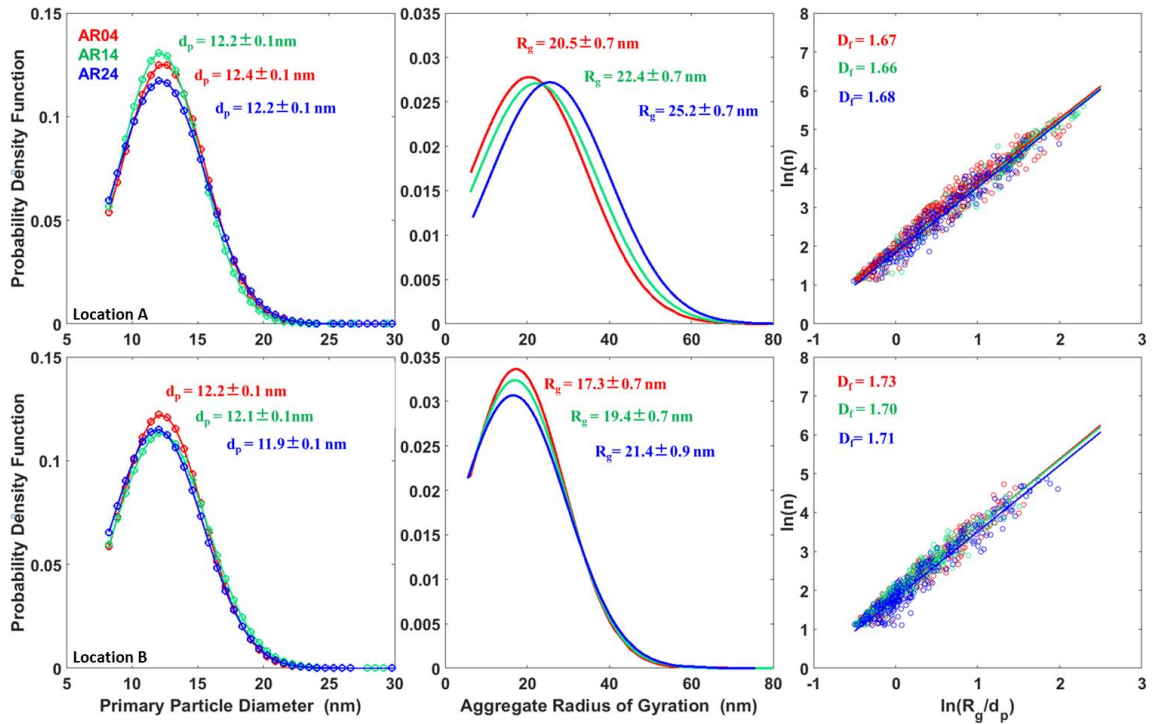


Figure 4.10: Probability density functions of soot primary particle diameter (d_p , left), aggregate radius of gyration (R_g , middle) and aggregate fractal dimension (d_f , right) for AR04, AR14 and AR24 fuels at location A (top) and location B (bottom) with 95% confidence error range

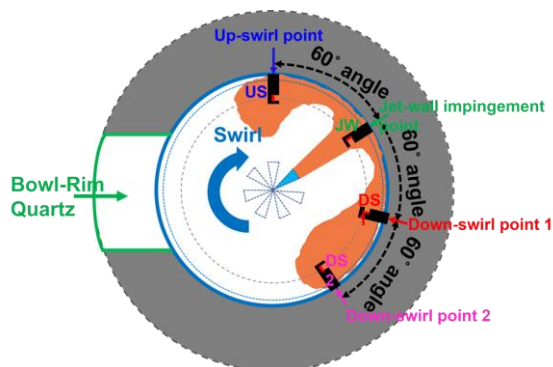
number of carbon layers. In contrast to the minimal change soot primary particle size, the aggregate R_g shows a significant increasing trend with an increase in fuel aromatics. This

means significantly enhanced aggregation of soot primary particles and small aggregates to form larger aggregates on account of increased aromatics in fuel. Interestingly, D_f shows only minor changes due to fuel aromatics, meaning similar compactness of soot aggregates with only the aggregate size growth identified as a major impact of aromatics in fuel.

Understanding of soot structure evolution of jet fuel with 24% aromatics

Table 5.1 Engine operating conditions for soot evolution study

Number of holes	1	
Injection pressure	70 MPa	
Fuel	AR24	Conventional diesel
Aromatics [vol%]	24%	
Injection duration	1286 μ s	
Injection timing	13 °CA bTDC	11 °CA bTDC
Injected fuel mass	9.0 mg	9.6 mg



44

tests. There were 15 injections conducted onto the sampling probes for both AR24 and diesel fuel, which ensured high number of soot aggregates enough for statistical data analysis while avoiding the bias associated with soot overloading. As a reference, a conventional diesel fuel is also investigated. The engine operating conditions used in this chapter are summarised in Table 5.1. The experiment is conducted in a single-jet condition for both AR24 and diesel with fixed injection duration of 1286 μs at 70 MPa. This is a simplified and fundamental environment, which avoids other potential impacts (*i.e.* complex jet-jet interactions) on soot evolution process. The impact of this research is directed at enhanced fundamental understandings, which will create a knowledge base required to develop a new-generation engine. The injection timing is 2 $^{\circ}\text{CA}$ retard for diesel due to higher cetane number. Similar with Chapter 4, this leads to fixed combustion phasing. The soot particles/aggregates are sampled from four different in-bowl locations simultaneously as illustrated in Figure 5.1. The sampling locations include jet-wall impingement point (JW), up-swirl point (US), down-swirl point 1 (DS1) and down-swirl point 2 (DS2), which are identified from high-speed soot luminosity images and planar laser induced incandescence (PLII) images.

5.1 In-cylinder pressure and soot luminosity images

Figure 5.2(left) shows the in-cylinder pressure traces for all single injection cases of both diesel and AR24 fuel. All 30 cycle pressure traces are plotted using grey lines together with the ensemble-averaged traces (coloured lines). The black and red colour indicate diesel and AR24, while the solid and dashed line indicate the traces recorded with and without four soot sampling probes installed. The in-cylinder pressure traces show that the start of combustion (SOC) is matched well between diesel and AR24 fuel at about 3 $^{\circ}\text{CA}$ aTDC. This was achieved by setting the injection timing of diesel two crank angles later, given its cetane number is higher than AR24. This led to longer ignition delay and higher

pre-mixing time for AR24, and thus higher peak pressure is measured. This difference

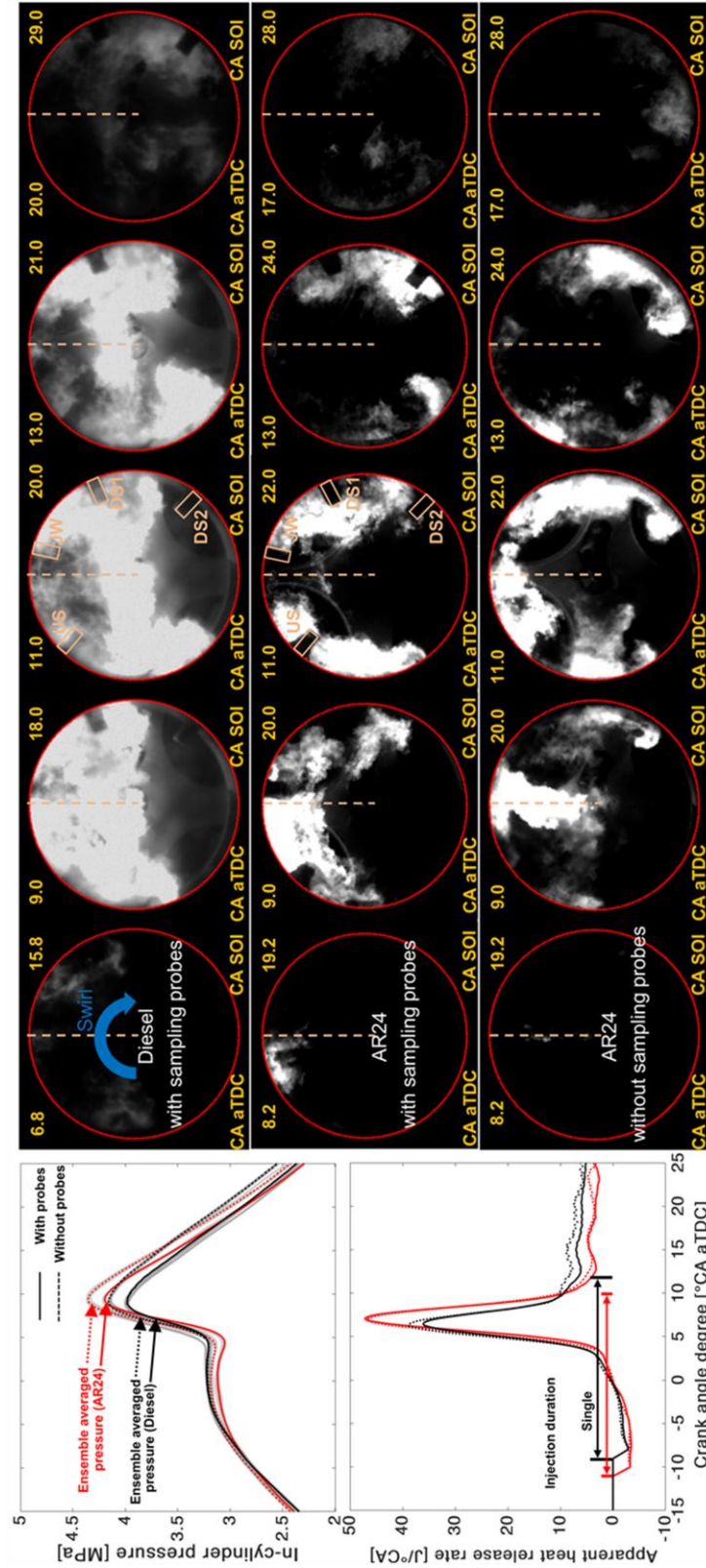


Figure 5.2: In-cylinder pressure, apparent heat release rate and selected high-speed soot luminosity images of a single injection condition for diesel and AR24 fuels. For AR24, the images are shown for both with and without the soot sampling probes

well exceeds the cyclic variations. When the sampling probes are installed, the pressure becomes lower than the no probe condition, as the heat loss increases; however, the combustion phasing is matched well regardless of fuel or probe installation conditions. From the apparent heat release rate (aHRR) shown below the pressure plot, it is also seen that the aHRR is very similar despite the added soot sampling probes. During the main combustion occurring between 3 and 10 °CA aTDC, the aHRR profiles are almost identical regardless of the probe installation condition. For diesel, the late-cycle aHRR is measured lower due to increased heat loss through the soot sampling probes but this is not significant for AR24 as it is more premixed combustion with much lower late-cycle aHRR. It is noted matching all key engine combustion parameters such as the peak pressure/aHRR, start of combustion and combustion phasing are not possible when the injected total energy is fixed for two different fuels as in the present study. The measured differences in pressure and aHRR due both to fuel and sampling probes will be carefully considered for the analysis of soot morphology and internal structure in the following sections.

Some selected individual cycle soot luminosity images are shown in Figure. 5.2(right), which correspond to diesel and AR24 combustion with the soot sampling probes installed (top two rows). At the bottom row, the soot luminosity images without the sampling probes are also presented. In each image, the crank angle timing (°CA aTDC) and corresponding time after the start of actual injection (°CA aSOI) are annotated. The red circle marks the piston bowl wall, and the yellow vertical line indicates the single jet axis. In the middle images, the locations of the four soot sampling probes (US, JW, DS1 and DS2) are illustrated to show the sampling points with respect to the flame development. The diesel images indicate, by 6.8 °CA aTDC, the soot signals develop in three sampling points of JW, US and DS1 as the jet impinges on the JW and travels along the bowl wall

towards both US and DS1 directions. Between 9 and 13 °CA aTDC, the up-swirl side of the wall jet shows a turbulent ring vortex formation due to the jet-swirl interaction while a volume of soot luminosity signals also reaches DS2 sampling point on the down-swirl side. As will be shown later, the soot sampling was successful for all four points. During the initial tests, the soot sampling probe was also placed further downstream of US location equivalent to DS2, which however showed no sampled soot particles due to intense oxidation. Therefore, this sampling point was excluded. At 20 °CA aTDC, the soot luminosity signals become very weak with some remaining signals causing a shadow of DS2 sampling probe.

Compared to the diesel flames, the AR24 flames exhibit less intense soot luminosity signals, which are found mostly along the bowl wall. It was noted the peak pressure and aHRR were measured higher for AR24, which might suggest higher ambient gas temperature and thus higher soot formation conditions. However, it was the longer ignition delay and increased premixing that caused lower sooting condition for AR24. This means the higher pressure/aHRR conditions set for the soot sampling would not affect the sampled soot structure negatively; that is, the sampled soot of AR24 would not be biased towards higher formation condition.

Importantly, the soot luminosity signals pass through all four soot sampling probes, suggesting successful thermophoretic particle sampling. Between with and without sampling probe conditions of AR24, a slightly decelerated penetration of the flame is observed on the down-swirl side of the wall jet. When the wall-jet momentum was strong as the flame travels through JW, US and DS1, the presence of the sampling probes appear not to affect the sooting flame development significantly. However, for DS2 point, a significantly reduced jet momentum meant decelerated penetration. For example, the no probe case shows a clear turbulent ring vortex formation on the down-swirl side of the jet between 11 and 13 °CA aTDC. By contrast, with DS2 on the path of the sooting flame development, the penetration was interfered and thus no such ring vortex formation

occurred. It is a limitation of the intrusive soot sampling used in the present study, and thus the result of DS2 point will be carefully considered in interpreting sampled soot particles in the following sections.

5.2 Planar laser induced incandescence (PLII) images

Figure 5.3 shows PLII images for both diesel and AR24 fuel at two different laser planes. The images were taken between 8 and 15 °CA aTDC with one crank angle increment, corresponding to the soot luminosity signal period shown in Figure 5.2. These are selected individual cycle images from 20 images taken at each crank angle. Similar with the previous studies [95,106], the selection of the present images was systematically performed such that each image was compared using the calculated cross-correlation coefficient until one returning the highest similarity with the ensemble-averaged image is found.

The images in Figure 5.3 show that the PLII signals are first detected from the jet-wall impingement point before the end of fuel injection. They then flow along the bowl wall to form a wall-jet structure. It is noted the diesel fuel had a higher amount of soot, which caused significant beam attenuation [89,106]. This confirms high soot formation shown in the soot luminosity images in Figure 5.2 but the PLII images cannot provide useful information about the soot sampling locations. In contrast to the diesel fuel, AR24 exhibits minimal beam attenuation due to lower soot formation. Figure 5.3 shows a clear wall-jet structure at both laser planes, and all four soot sampling probes illustrated in the middle images suggest successful thermophoretic particle sampling. From the PLII signal distribution and its temporal evolution, it is also thought that the selected JW, US, DS1 and DS2 sampling points would present soot particles along the penetrating flame path.

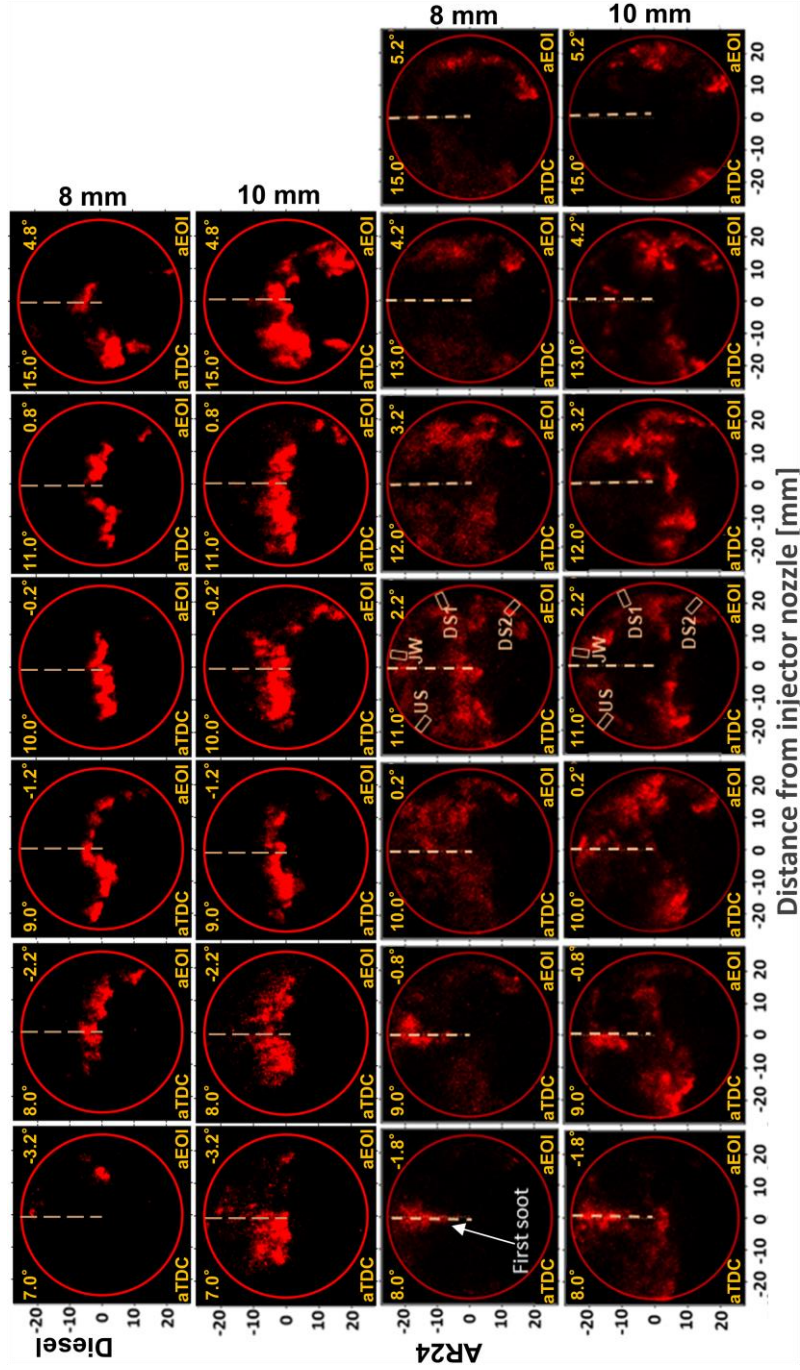


Figure 5.3: Selected planar laser induced incandescence (PLII) images of diesel and AR24 fuel with a single injection. The PLII images are shown for the different laser planes below the cylinder head

5.3 Soot particle morphology analysis

Figure 5.4 shows some example TEM images of both diesel and AR24 soot at the four sampling locations. A total of 10 and 30 TEM images were taken under 30k and 100k magnification settings, which are shown at the top and bottom row, respectively. The 500-nm and 200-nm scale bars are annotated at the top-left image of each magnification setting. Between these soot TEM images, soot aggregates count plots are presented. This result is based on 30k magnification TEM images to use a sufficiently high number of samples. The corresponding 100k magnification TEM images provide visual information

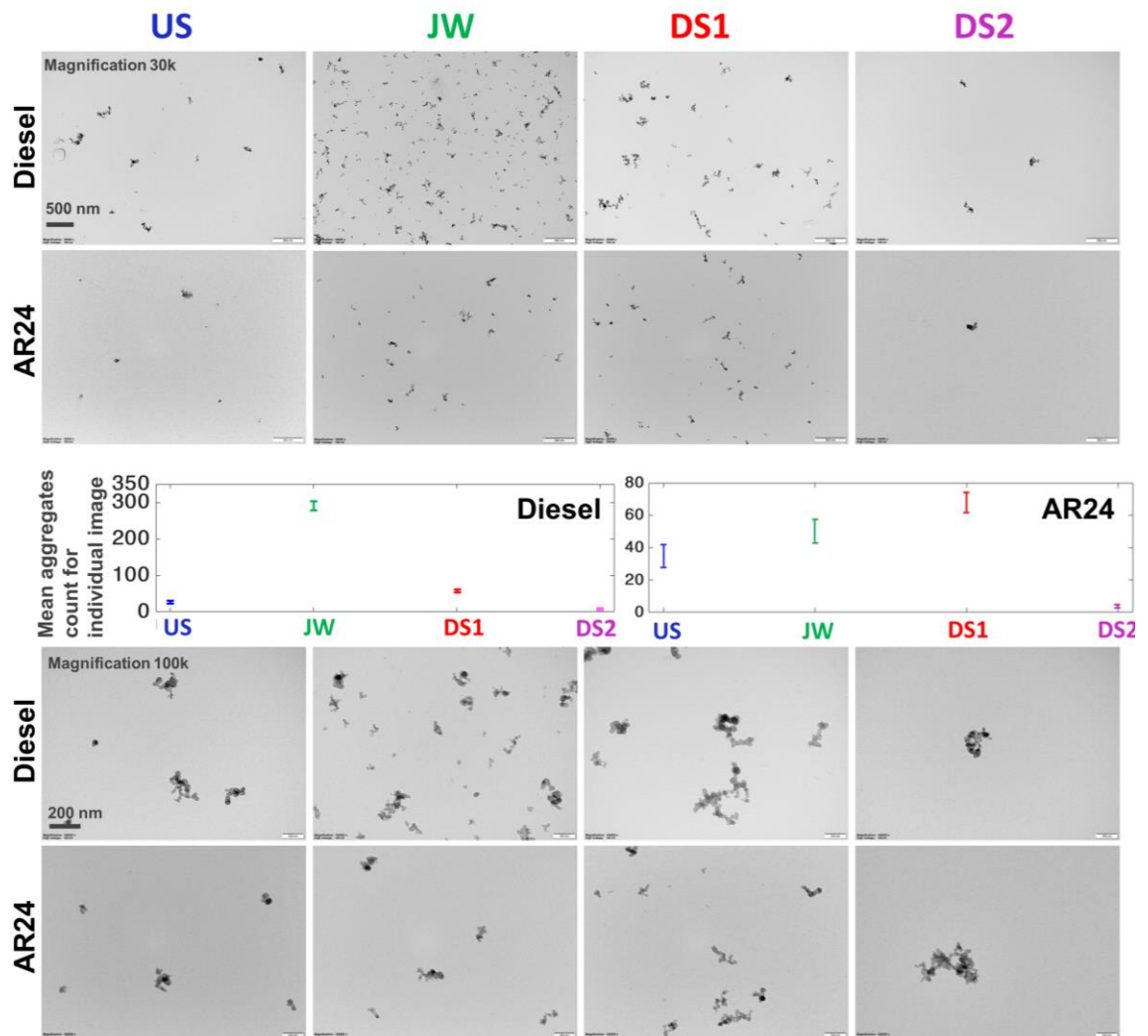


Figure 5.4: Example TEM images of the four sampling locations for each of diesel and AR fuels. A 30k TEM magnification is used for the soot aggregate number counting with the mean value plotted with error margins of 95% confidence

about soot aggregate shapes and structures. The TEM images and the soot aggregate number counts confirm much higher soot formation for diesel compared to AR24 fuel, particularly at JW point – *i.e.* when a large amount of soot aggregates form in rich mixtures upon the jet impingement on the wall. As shown previously in Figure 5.2, the fixed fuel mass and combustion phasing conditions used in this study led to higher pressure and aHRR peaks for AR24. The soot TEM images in Figure 5.4 indicate the sampled soot particles are not affected by potentially higher ambient gas temperature. AR24 presented more premixed combustion due to longer ignition delay, which was consistent with lower soot luminosity and PLII signals and is now with a lower amount of sampled soot aggregates. However, the more premixed combustion condition alone is not sufficient to explain an order of magnitude lower soot aggregate counts of AR24. Diesel is a multi-component fuel with a range of hydrocarbons and is much less volatile compared to kerosene based AR24. It is therefore both a more premixed combustion condition and a fuel molecular structure less prone to soot formation to cause much less soot aggregates for AR24. Therefore, analysing diesel soot samples together with AR24 soot is useful in investigating soot structure evolution along the flame development path with relatively higher and lower sooting levels.

The sampled soot amount shows a significant change as the sooting flame travels from JW point to US point. For both diesel and AR24, the soot reduction is significant because the swirl countered with the wall-jet head to promote mixing and soot oxidation [44]. A marked reduction is shown for diesel with over 300 sampled soot aggregates per TEM image at JW point decreased to only around 10 soot aggregates at US point. The JW to US point reduction rate is much less for AR24 with 50 soot aggregates to 35, suggesting the influence of soot aggregates structure on the soot oxidation rate. For example, the 100k magnification TEM images in Figure 5.4 display more agglomerated and compact

soot aggregates at US point for AR24, which would be harder to be broken up and oxidised.

Between JW and DS1 point, the diesel soot also shows a significant decrease in the aggregate number count similar with US point. However, this side of the flame travels in the same direction of a swirl flow and thus the soot oxidation was less significant [44,45]. In fact, the TEM images of diesel show soot aggregates are much larger than those sampled at JW point, suggesting soot aggregation. AR24 soot shows a similar trend with some aggregates of DS1 point are larger than those of JW point. However, it appears the soot aggregate count does not decrease as the AR24 flame penetrates from JW point to DS1 point - the number count difference is within the error margin, suggesting the continued soot formation.

The soot aggregates sampled from DS2 point show the lowest number counts for both diesel and AR24, indicating at this late combustion stage, the soot oxidation was significant regardless of fuel types [8,43–45]. The 30k magnification TEM images show only two to three soot aggregates as a product of complex soot formation and oxidation in the earlier stages. Previously, the interference of sooting flames by the sampling probes was raised as a concern; however, the continued soot structure change suggests the results were not biased and even if there was a measurable influence, it would only make the observed trend clearer – *i.e.* the DS2 soot would be even more oxidised if there were no interference.

The 100k magnification images of Figure 5.4 were post processed to quantify key morphology parameters. The results are shown in Figure 5.5 for probability density functions (PDFs) of radius of gyration of the soot aggregates (R_g , top row), soot primary particle diameter (d_p , middle row). The numbers noted next to each PDF line are the mean

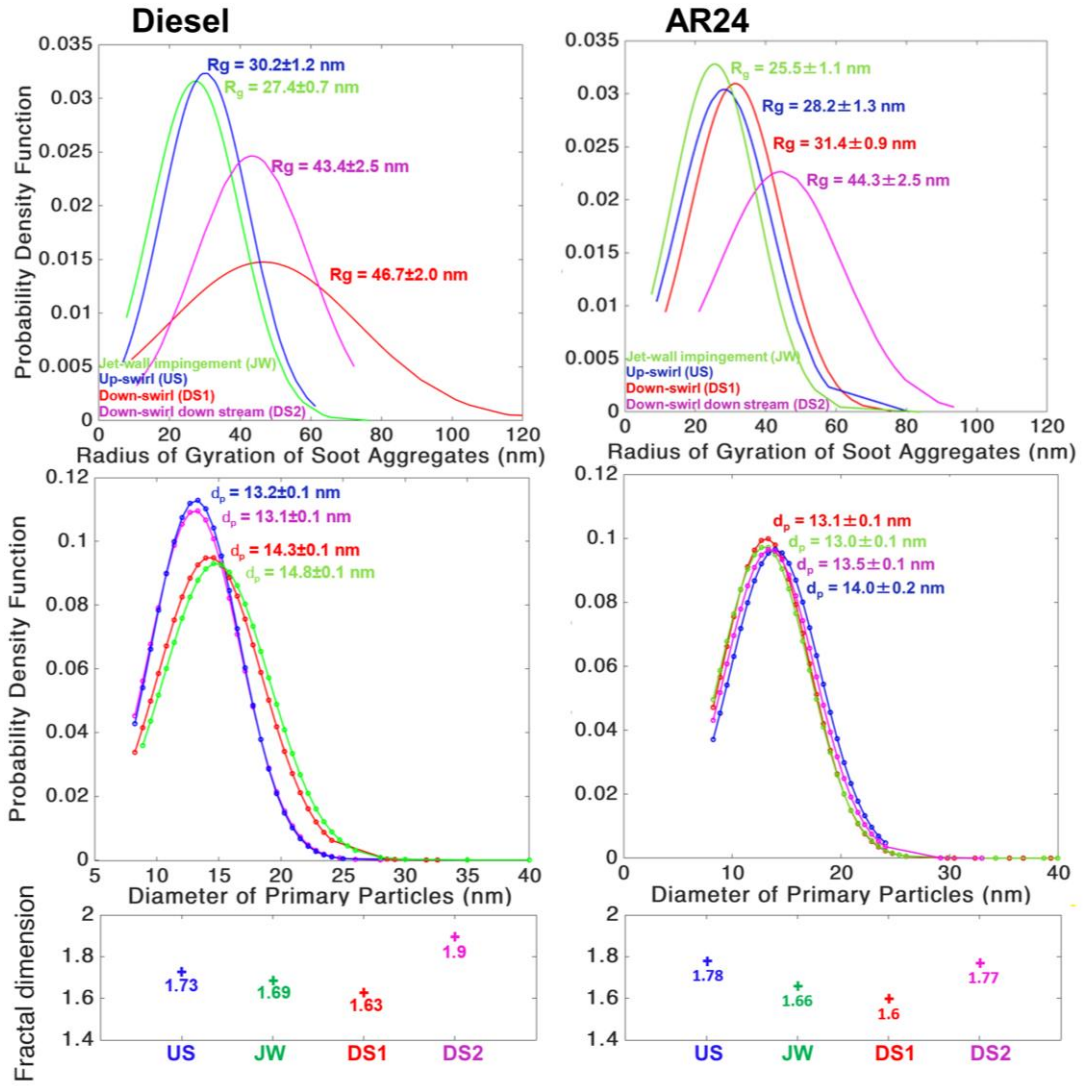


Figure 5.5: Size distribution of the soot aggregate radius of gyration and primary particles of the four sampling locations. The results are shown for diesel (left) and AR24 fuel (right). The estimated fractal dimension is shown at the bottom

values with the error bars of 95% confidence. At the bottom row, the fractal dimension (d_f) of the soot aggregates is presented. From Figure 5.5, it is seen the overall R_g of diesel soot is higher than AR24, which is consistent with higher soot formation shown in the soot luminosity and PLII images. This means not only more soot aggregates are formed but also they are larger for diesel.

As the expected soot oxidation occurred between JW and US point, R_g shows a slight increase, which is primarily due to the elimination of small soot aggregates (see Figure 5.4). The remaining soot aggregates are more compact and agglomerated as indicated by increased d_f . The diesel d_p shows a measurable reduction due to significant soot oxidation, as previously reported [8]. However, the AR24 d_p shows only minor changes from JW to US point as well as to other sampling points with very similar PDF profiles. This might indicate AR24 soot was already mature and oxidised at JW point or new soot primary particle formation continued to occur at other sampling points. As the flame travels from JW to DS1 point and then to DS2 point, a significant increase in R_g and d_f is observed for both fuels. For diesel, d_p also shows a decreasing trend, which can be explained by continued soot oxidation [8]. In the case of AR24 fuel, the continued increase of R_g is clearer while d_p shows no significant difference. This requires further analysis using the high-resolution TEM images showing soot internal structures.

5.4 Soot internal structure analysis

The continued reduction of d_p , increase of R_g and reduced aggregate number counts observed for diesel are consistent with the previous studies performed in the same engine but using a single point soot sampler [43–45]. This was explained by continued soot oxidation of primary particles, merger of soot aggregates and oxidation occurring in the outer region of soot aggregates as well as elimination of small aggregates. The soot oxidation status shown in the carbon-layer fringes supported the continued oxidation of soot primary particles too [8,44]. However, the AR24 jet fuel of the present study showed no change in d_p at any sampling points. To discuss this unexpected trend, high resolution TEM images of AR24 were post processed to extract carbon-layer fringes and to perform soot internal structure analysis.

Figure 5.6 shows example HR-TEM images with a 5-nm scale bar annotated at the top left image (top row). The corresponding two-dimensional concentricity maps are overlaid on the HR-TEM images as shown in the middle. The frequency distribution plots are presented at the bottom of Figure 5.6, which are based on five soot primary particles for each of four sampling points. Between JW and US point, the lower concentricity measured for JW point due to a disordered amorphous core structure increases as the carbon-layer fringes formed a more centred core-shell structure, indicating significant soot oxidation. This leads to increased concentricity frequency in the 0.5~0.6 range as well as 0.3~0.4 range to show a clear distinction between the inner core and outer shell. The same trend is observed between JW and DS1/DS2 points with much clearer core-

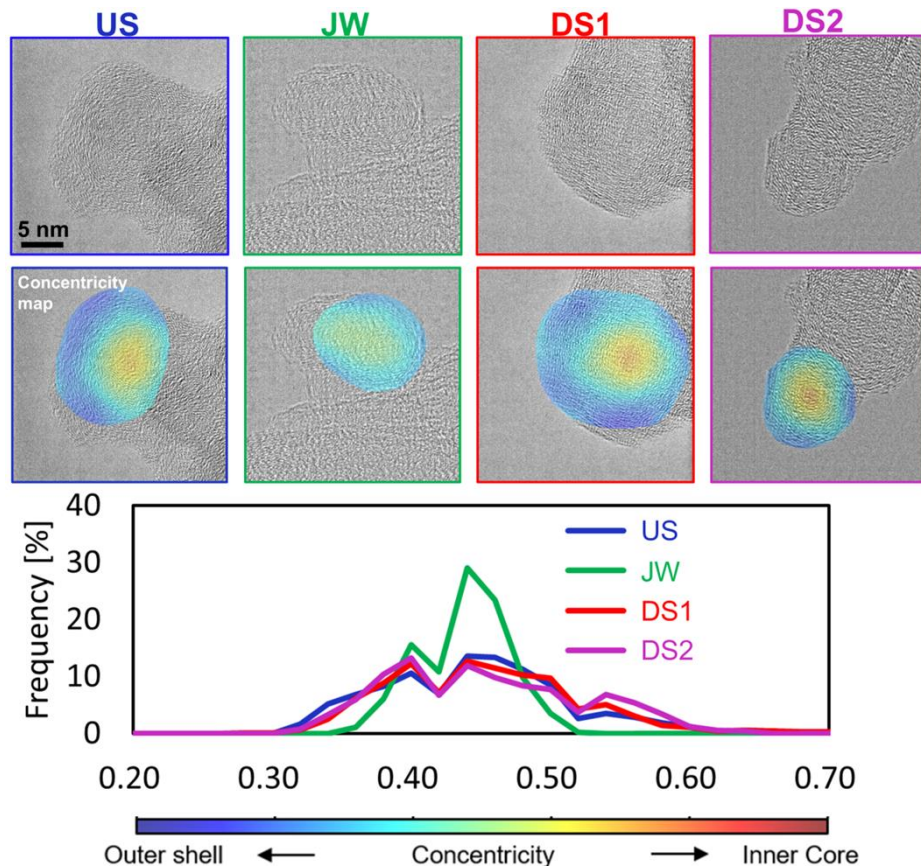


Figure 5.6: Example HR-TEM images of a soot primary particle and overlaid concentricity colormap for four sampling locations of AR24 fuel. The frequency plot of the concentricity calculated from five soot primary particles is shown at the bottom

shell structures shown at DS2 point. In the 0.5~0.6 concentricity range, DS2 point shows the maximum frequency.

The carbon-layer fringes were further processed as shown in Figure. 5.7 for fringe length (L_f), tortuosity (T_f) and fringe-to-fringe separation (d). The skeleton images shown in the middle row are carbon-layer fringes identified from the marked region of the HR-TEM images (top row). The PDFs at the bottom row are a result of ten HR-TEM images with 3000 carbon fringes and over 1000 fringe pairs for each sampling point. The results show that JW point has the shortest L_f with the highest T_f and larger d , indicating the soot at this point is at an early stage of formation with immature status, consistent with the concentricity results. From JW to US point, L_f increases while T_f and d decrease meaning significant oxidation [8].

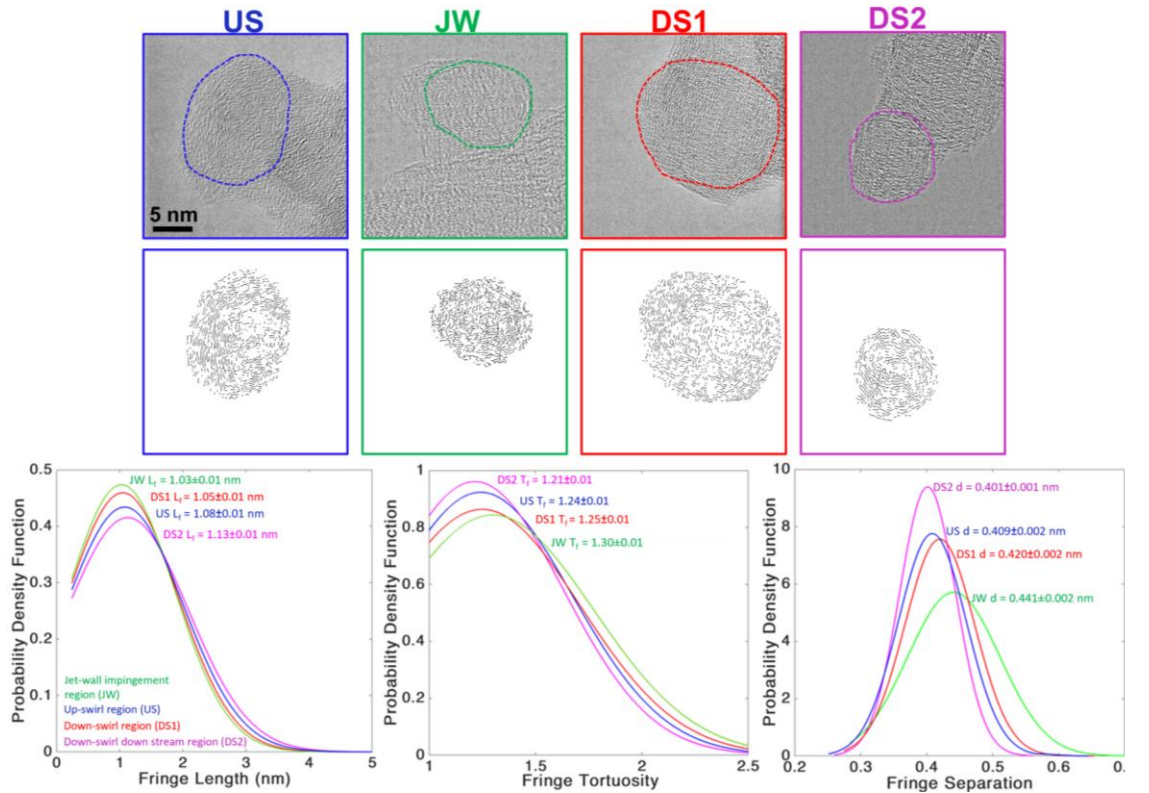


Figure 5.7: Example HR-TEM images of AR24 fuel at varied sampling locations (top). Shown in the middle are the corresponding carbon-layer fringes. The PDF profiles of the fringe length, tortuosity and separation are presented at the bottom row

On the down-swirl side, the fringe parameters change between JW to DS1 point is less significant than that between JW and US point due to co-flow conditions [44,45]. In the soot aggregates images (Figure. 5.4), DS1 point showed continued soot growth evidenced by higher R_g due to aggregation. During this soot growth, however, both the concentricity (Figure. 5.6) and fringe parameters (Figure. 5.7) show more graphitised soot internal structures, meaning the oxidation also continued. A recent study provided additional fundamental insight about the soot formation/oxidation occurring within the developing flame [36]. By comparing the soot sampled from the flame periphery and flame core regions, it was suggested the highly agglomerated and compact soot aggregates found at the late stage of diesel combustion are the ones stemmed from the flame core experiencing very limited oxidation. More graphitised particle status than JW soot indicates the DS1 soot is not decoupled from the JW soot but it is part of the soot evolution along the flame development path.

After the intermediate condition between JW and DS1 point, as the sooting flame reached DS2 point, it shows the highest L_f and T_f and the smallest d among the tested four sampling points. This, together with a compact soot aggregate structure (Figure 5.4 and 5), suggests the most oxidised status of soot. Therefore, it is plausible to explain that the soot oxidation continued from the original formation point of JW to US and to DS1/DS2 despite no significant variation measured in the soot primary particle size (d_p). It was thought that, for lower sooting fuels such as AR24, the change in soot primary particle was so small that was hard to be captured in the standard TEM images. It was only high-resolution TEM that could reveal measurable differences in the sub-nano scale carbon-layer fringes.

Chapter 6.

Conclusion

The effect of fuel aromaticity on in-flame soot processes in a single-cylinder optical engine has been investigated using three custom-made jet fuels achieving aromatic content variations independent of other fuel properties. From a suite of optical diagnostics ranging from cool flame, OH* chemiluminescence and soot luminosity as well as HCHO-PLIF and soot-PLII imaging, the reactions and soot distributions were visualised. The direct soot particle sampling was also performed, and their internal structure and morphology were analysed. Several major findings have been achieved as follows:

- Due to the use of custom-made jet fuels with systematic variation of aromatics, the measured in-cylinder pressure, aHRR and cool-flame/ OH* chemiluminescence as well as HCHO-PLIF show little change in signal distribution and intensity. This provided an excellent opportunity to exclusively study the effect of aromatics on soot formation.
- From soot luminosity and PLII images, the soot distribution and development pattern were found not to change due to fuel aromatics. However, a higher aromatic fuel shows earlier soot inception and higher growth rate, leading to higher peak soot and remaining soot.
- Detailed analysis of sampled soot particles showed the carbon layers grow more for a higher aromatic fuel, which forms more mature, graphitised internal structures within

the soot primary particles. This is related to higher PAH formation, supported by the measured PAH interference to the HCHO-PLIF signals.

- The increased soot formation for a higher aromatic fuel is closely linked to increased soot aggregates size. Both the TEM images and size distribution plots indicate significantly enhanced soot aggregation caused by higher aromatics.

To understand the soot evolution of surrogate jet fuels, the AR24 fuel has been further investigated by placing multiple thermophoretic sampling probes within the piston bowl. High-speed soot luminosity imaging and planar laser induced incandescence performed for AR24 and a conventional diesel fuel as a baseline were used to identify four key sampling points along the flame path including a jet-wall impingement point (JW), an up-swirl point (US), a down-swirl point 1 (DS1) and a down-swirl point 2 (DS2) with 60° spacing angle. The main findings from this part of study are summarised as follows:

- The sooting flame in a small-bore engine used in the present study has a wall-interacting jet flame structure with the jet impinging on the wall forming a fuel rich mixture at JW point. The soot luminosity and LII signals are observed at US point as well as DS1 and DS2 point as the wall flame continues to develop.
- From the soot TEM images and statistical analysis of soot aggregate structures, a high number of small soot aggregates at JW point are observed due to initial soot formation. Between JW point and US point, the soot aggregates become larger while the number count decreases, indicating soot oxidation induced elimination of aggregates. On the down-swirl side (DS1 point), the aggregate size also increases but the number count does not decrease, suggesting the aggregation occurring while the new soot formation continued.

- At DS2 point, only large aggregates with compact structures are observed indicating the particles survived intense oxidation were sampled, and they could be even more oxidised if no probes were installed. A further 60° downstream of US point was also tested, which returned no soot sample due to significant soot oxidation.
- The soot primary particle size shows a decreasing trend along the flame path in the case of diesel, but the variation is very small for AR24. The HR-TEM results showed that the core-shell particle structure becomes clearer and the carbon-layer fringe-to-fringe gap decreases during the flame penetration, indicating the soot sampled from each location is not decoupled from the previous location but is part of soot evolution along the flame development path. This also suggests the soot oxidation continued although it was not shown clearly on the soot particle size. This is related to lower soot formation of AR24 compared to diesel with the soot formed at JW point more oxidised in the first place and thus the following oxidation made relatively weaker impact.
- From the soot sampling and structure study performed in a small-bore compression ignition engine fuelled with a surrogate jet fuel, the in-flame soot evolution is characterised by high formation of small aggregates at JW point, simultaneous aggregation and oxidation at US and DS1 point with the latter more prone to aggregation, and significant oxidation at DS2 point.

6.1 Future work

From the experiment, the sole impact of fuel aromaticity on soot morphology and nanostructure is better understood. From previous studies, the kind of aromatics and the benzene ring number of the aromatic in the fuel still play an important role in the combustion and in-cylinder soot process. Since soot emission is still the major drawback of diesel combustion, further study could focus on the impact of varying aromatic

molecule structures on in-cylinder soot. Regarding the soot investigation, a comparison between the TEM and time resolved LII obtained soot morphology parameters is suggested as a future work, which could further prove the accuracy of morphology values. Other advanced techniques could also be applied for more detailed soot research, such as the EELS (electron energy loss spectroscopy) technique for the carbon hybridization of soot.

The diagnostic for studying different combustion process in current study is the PLII and PLIF imaging. In the future study, the phosphor particles could be used in the diesel engine with laser-induced phosphorescence to reflect the two-dimensional in-cylinder temperature and its distribution at different stages of the combustion process.

Given the components of the jet fuel surrogates and the experiments data all obtained in present study, some simulation work could be done to further acknowledge the combustion processes for this set of jet fuels. For example, performing the chemical kinetic combustion modelling with major components of the surrogates for the further understanding of the combustion phases.

Lastly, in this study, the multi-location soot sampling method is proven to reflect the structural changes of soot evolution for different fuels. It is worthwhile to investigate the soot structural evolution of cleaner energy sources, such as biofuels, with the same sampling method, providing insight knowledge into soot reduction.

Reference

- [1] ICCT Europe. European Vehicle market statistics. 2021.
- [2] Bieker G, Tietge U, Rodriguez F, Mock P. European vehicle market statistics, 2019/2020 | International Council on Clean Transportation n.d. <https://theicct.org/publications/european-vehicle-market-statistics-20192020> (accessed July 19, 2021).
- [3] Saddler H. National Energy Emissions Audit: October 2019 - The Australia Institute n.d. <https://australiainstitute.org.au/report/national-energy-emissions-audit-october-2019/> (accessed May 20, 2022).
- [4] Reducing Emissions from Non-road Diesel Engines. 2014.
- [5] Guo J, Kauppinen T, Kyyrönen P, Heikkilä P, Lindbohm M-L, Pukkala E. Risk of esophageal, ovarian, testicular, kidney and bladder cancers and leukemia among finnish workers exposed to diesel or gasoline engine exhaust. *Int J Cancer* 2004;111:286–92. <https://doi.org/10.1002/ijc.20263>.
- [6] Kook S, Bae C, Miles PC, Choi D, Pickett LM. The influence of charge dilution and injection timing on low-temperature diesel combustion and emissions. *SAE Tech Pap* 2005. <https://doi.org/10.4271/2005-01-3837>.
- [7] Tree DR, Svensson KI. Soot processes in compression ignition engines. *Prog Energy Combust Sci* 2007;33:272–309. <https://doi.org/10.1016/j.pecs.2006.03.002>.
- [8] Rao L, Zhang Y, Kim D, Su HC, Kook S, Kim KS, et al. Effect of after injections on late cycle soot oxidation in a small-bore diesel engine. *Combust Flame* 2018;191:513–26. <https://doi.org/10.1016/j.combustflame.2018.02.014>.
- [9] Zhang R, Kook S. Influence of fuel injection timing and pressure on in-flame soot particles in an automotive-size diesel engine. *Environ Sci Technol* 2014;48:8243–50. <https://doi.org/10.1021/es500661w>.
- [10] Härtl M, Seidenspinner P, Jacob E, Wachtmeister G. Oxygenate screening on a

- heavy-duty diesel engine and emission characteristics of highly oxygenated oxymethylene ether fuel OME1. *Fuel* 2015;153:328–35. <https://doi.org/10.1016/j.fuel.2015.03.012>.
- [11] Saggese C, Singh A V., Xue X, Chu C, Kholghy MR, Zhang T, et al. The distillation curve and sooting propensity of a typical jet fuel. *Fuel* 2019;235:350–62. <https://doi.org/10.1016/j.fuel.2018.07.099>.
- [12] Zhang T, Zhao L, Thomson MJ. Effects of n-propylbenzene addition to n-dodecane on soot formation and aggregate structure in a laminar coflow diffusion flame. *Proc Combust Inst* 2017;36:1339–47. <https://doi.org/10.1016/j.proci.2016.05.026>.
- [13] An YZ, Li X, Teng SP, Wang K, Pei YQ, Qin J, et al. Development of a soot particle model with PAHs as precursors through simulations and experiments. *Fuel* 2016;179:246–57. <https://doi.org/10.1016/j.fuel.2016.03.100>.
- [14] Leermakers CAJ, Musculus MPB. In-cylinder soot precursor growth in a low-temperature combustion diesel engine: Laser-induced fluorescence of polycyclic aromatic hydrocarbons. *Proc Combust Inst* 2015;35:3079–86. <https://doi.org/10.1016/j.proci.2014.06.101>.
- [15] Fu X, Aggarwal SK. Two-stage ignition and NTC phenomenon in diesel engines. *Fuel* 2015;144:188–96. <https://doi.org/10.1016/J.FUEL.2014.12.059>.
- [16] Jansons M, Brar A, Estefanous F, Florea R, Taraza D, Henein N, et al. Experimental investigation of single and two-stage ignition in a diesel engine. *SAE Tech Pap* 2008;2008:776–90. <https://doi.org/10.4271/2008-01-1071>.
- [17] Musculus MPB, Miles PC, Pickett LM. Conceptual models for partially premixed low-temperature diesel combustion. vol. 39. Elsevier Ltd; 2013. <https://doi.org/10.1016/j.pecs.2012.09.001>.
- [18] Battin-Leclerc F. Detailed chemical kinetic models for the low-temperature combustion of hydrocarbons with application to gasoline and diesel fuel surrogates. *Prog Energy Combust Sci* 2008;34:440–98. <https://doi.org/10.1016/j.pecs.2007.10.002>.

- [19] Zhang P, Ji W, He T, He X, Wang Z, Yang B, et al. First-stage ignition delay in the negative temperature coefficient behavior: Experiment and simulation. *Combust Flame* 2016;167:14–23. <https://doi.org/10.1016/j.combustflame.2016.03.002>.
- [20] Westbrook CK. Chemical kinetics of hydrocarbon ignition in practical combustion systems. *Proc Combust Inst* 2000;28:1563–77. [https://doi.org/10.1016/s0082-0784\(00\)80554-8](https://doi.org/10.1016/s0082-0784(00)80554-8).
- [21] Hildingsson L, Persson H, Johansson B, Collin R, Nygren J, Richter M, et al. Optical diagnostics of HCCI and low-temperature diesel using simultaneous 2-D PLIF of OH and formaldehyde. *SAE Tech Pap* 2004. <https://doi.org/2004-01-2949>.
- [22] Yang Z, Qian Y, Yang X, Wang Y, Wang Y, Huang Z, et al. Autoignition of n-butanol/n-heptane blend fuels in a rapid compression machine under low-to-medium temperature ranges. *Energy and Fuels* 2013;27:7800–8. <https://doi.org/10.1021/ef401774f>.
- [23] Kholghy M, Saffaripour M, Yip C, Thomson MJ. The evolution of soot morphology in a laminar coflow diffusion flame of a surrogate for Jet A-1. *Combust Flame* 2013;160:2119–30. <https://doi.org/10.1016/j.combustflame.2013.04.008>.
- [24] Reilly PTA, Gieray RA, Whitten WB, Ramsey JM. Direct observation of the evolution of the soot carbonization process in an acetylene diffusion flame via real-time aerosol mass spectrometry. *Combust Flame* 2000;122:90–104. [https://doi.org/10.1016/S0010-2180\(00\)00105-X](https://doi.org/10.1016/S0010-2180(00)00105-X).
- [25] Xi J, Yang G, Cai J, Gu Z. A Review of Recent Research Results on Soot: The Formation of a Kind of Carbon-Based Material in Flames. *Front Mater* 2021;8:1–6. <https://doi.org/10.3389/fmats.2021.695485>.
- [26] Kholghy MR, Veshkini A, Thomson MJ. The core-shell internal nanostructure of soot - A criterion to model soot maturity. *Carbon N Y* 2016;100:508–36. <https://doi.org/10.1016/j.carbon.2016.01.022>.
- [27] Jiang H, Li T, Wang Y, He P, Wang B. The evolution of soot morphology and

- nanostructure along axial direction in diesel spray jet flames. *Combust Flame* 2019;199:204–12. <https://doi.org/10.1016/j.combustflame.2018.10.030>.
- [28] Merchan-Merchan W, Abdihamzehkolaei A, Merchan-Breuer DA. Formation and evolution of carbon particles in coflow diffusion air flames of vaporized biodiesel, diesel and biodiesel-diesel blends. *Fuel* 2018;226:263–77. <https://doi.org/10.1016/j.fuel.2018.02.183>.
- [29] Michelsen HA, Schulz C, Smallwood GJ, Will S. Laser-induced incandescence: Particulate diagnostics for combustion, atmospheric, and industrial applications. *Prog Energy Combust Sci* 2015;51:2–48. <https://doi.org/10.1016/j.pecs.2015.07.001>.
- [30] Kholghy MR, Afarin Y, Sediako AD, Barba J, Lapuerta M, Chu C, et al. Comparison of multiple diagnostic techniques to study soot formation and morphology in a diffusion flame. *Combust Flame* 2017;176:567–83. <https://doi.org/10.1016/j.combustflame.2016.11.012>.
- [31] Sediako AD, Soong C, Howe JY, Kholghy MR, Thomson MJ. Real-time observation of soot aggregate oxidation in an Environmental Transmission Electron Microscope. *Proc Combust Inst* 2017;36:841–51. <https://doi.org/10.1016/J.PROCI.2016.07.048>.
- [32] Neoh KG, Howard JB, Sarofim AF. Effect of oxidation on the physical structure of soot. *Symp Combust* 1985;20:951–7. [https://doi.org/10.1016/S0082-0784\(85\)80584-1](https://doi.org/10.1016/S0082-0784(85)80584-1).
- [33] Hurt RH, Crawford GP, Shim HS. Equilibrium nanostructure of primary soot particles. *Proc Combust Inst* 2000;28:2539–46. [https://doi.org/10.1016/S0082-0784\(00\)80670-0](https://doi.org/10.1016/S0082-0784(00)80670-0).
- [34] Toth P, Palotas AB, Ring TA, Eddings EG, Vander Wal R, Lighty JAS. The effect of oxidation pressure on the equilibrium nanostructure of soot particles. *Combust Flame* 2015;162:2422–30. <https://doi.org/10.1016/J.COMBUSTFLAME.2015.02.009>.
- [35] Vander Wal RL, Tomasek AJ. Soot oxidation: Dependence upon initial

- nanostructure. *Combust Flame* 2003;134:1–9. [https://doi.org/10.1016/S0010-2180\(03\)00084-1](https://doi.org/10.1016/S0010-2180(03)00084-1).
- [36] Aizawa T, Toyama Y, Kusakari R. Quantitative high-resolution transmission electron microscopy nanostructure analysis of soot oxidized in diesel spray flame periphery. *Int J Engine Res* 2020;22:1579–91. <https://doi.org/10.1177/1468087420914480>.
- [37] Rao L, Zhang Y, Kook S, Kim KS, Kweon CB. Understanding the soot reduction associated with injection timing variation in a small-bore diesel engine. *Int J Engine Res* 2019. <https://doi.org/10.1177/1468087419868058>.
- [38] Sun C, Martin J, Boehman AL. Nanostructure and reactivity of soot produced from a turbodiesel engine using post injection. *Proc Combust Inst* 2019;37:1169–76. <https://doi.org/10.1016/J.PROCI.2018.06.101>.
- [39] Sun C, Martin J, Boehman AL. Impacts of advanced diesel combustion operation and fuel formulation on soot nanostructure and reactivity. *Fuel* 2020;276. <https://doi.org/10.1016/j.fuel.2020.118080>.
- [40] Zhu J, Lee KO, Yozgatligil A, Choi MY. Effects of engine operating conditions on morphology, microstructure, and fractal geometry of light-duty diesel engine particulates. *Proc Combust Inst* 2005;30 II:2781–9. <https://doi.org/10.1016/j.proci.2004.08.232>.
- [41] Potenza M, Milanese M, de Risi A. Effect of injection strategies on particulate matter structures of a turbocharged GDI engine. *Fuel* 2019;237:413–28. <https://doi.org/10.1016/j.fuel.2018.09.130>.
- [42] Jain A, Singh AP, Agarwal AK. Effect of fuel injection parameters on combustion stability and emissions of a mineral diesel fueled partially premixed charge compression ignition (PCCI) engine. *Appl Energy* 2017;190:658–69. <https://doi.org/10.1016/J.APENERGY.2016.12.164>.
- [43] Zhang Y, Kim D, Rao L, Zhang R, Kook S, Kim KS, et al. The soot particle formation process inside the piston bowl of a small-bore diesel engine. *Combust Flame* 2017;185:278–91. <https://doi.org/10.1016/j.combustflame.2017.07.028>.

- [44] Zhang Y, Kim D, Rao L, Kook S, Kim KS, Kweon CB. In-flame soot particle structure on the up- and down-swirl side of a wall-interacting jet in a small-bore diesel engine. *Proc Combust Inst* 2019;37:4847–55. <https://doi.org/10.1016/j.proci.2018.07.104>.
- [45] Zhang R, Kook S. Structural evolution of soot particles during diesel combustion in a single-cylinder light-duty engine. *Combust Flame* 2015;162:2720–8. <https://doi.org/10.1016/j.combustflame.2015.04.008>.
- [46] Rao L, Zhang Y, Kook S, Kim KS, Kweon CB. Understanding in-cylinder soot reduction in the use of high pressure fuel injection in a small-bore diesel engine. *Proc Combust Inst* 2019;37:4839–46. <https://doi.org/10.1016/j.proci.2018.09.013>.
- [47] Lee C fon, Wu Y, Wu H, Shi Z, Zhang L, Liu F. The experimental investigation on the impact of toluene addition on low-temperature ignition characteristics of diesel. *Fuel* 2019;254:115580. <https://doi.org/10.1016/j.fuel.2019.05.163>.
- [48] Han D, Duan Y, Zhai J. Autoignition comparison of n-dodecane/benzene and n-dodecane/toluene blends in a constant volume combustion chamber. *Energy and Fuels* 2019;33:5647–54. <https://doi.org/10.1021/acs.energyfuels.9b00451>.
- [49] da Silva G, Rafiq Hamdan M, Bozzelli JW. Oxidation of the benzyl radical: Mechanism, thermochemistry, and kinetics for the reactions of benzyl hydroperoxide. *J Chem Theory Comput* 2009;5:3185–94. <https://doi.org/10.1021/ct900352f>.
- [50] Hwang W, Dec J, Sjöberg M. Spectroscopic and chemical-kinetic analysis of the phases of HCCI autoignition and combustion for single- and two-stage ignition fuels. *Combust Flame* 2008;154:387–409. <https://doi.org/10.1016/j.combustflame.2008.03.019>.
- [51] Kidoguchi Y, Yang C, Kato R, Miwa K. Effects of fuel cetane number and aromatics on combustion process and emissions of a direct-injection diesel engine. *JSAE Rev* 2000;21:469–75. [https://doi.org/10.1016/S0389-4304\(00\)00075-8](https://doi.org/10.1016/S0389-4304(00)00075-8).
- [52] Kee SS, Mohammadi A, Kidoguchi Y, Miwa K. Effects of aromatic hydrocarbons on fuel decomposition and oxidation processes in diesel combustion. *SAE Tech*

Pap 2005;114:765–72. <https://doi.org/10.4271/2005-01-2086>.

- [53] Yehia OR, Reuter CB, Ju Y. Kinetic effects of n-propylbenzene on n-dodecane diffusion cool flame extinction. 10th US Natl Combust Meet 2017;2017-April:1–6.
- [54] Talibi M, Hellier P, Ladommatos N. Impact of increasing methyl branches in aromatic hydrocarbons on diesel engine combustion and emissions. *Fuel* 2018;216:579–88. <https://doi.org/10.1016/J.FUEL.2017.12.045>.
- [55] Zhang T, Thomson MJ. A numerical study of the effects of n-propylbenzene addition to n-dodecane on soot formation in a laminar coflow diffusion flame. *Combust Flame* 2018;190:416–31. <https://doi.org/10.1016/j.combustflame.2017.12.019>.
- [56] Chu C, Thomson MJ. The effects of naphthalene-addition to alkylbenzenes on soot formation. *Combust Flame* 2020;215:169–83. <https://doi.org/10.1016/j.combustflame.2020.01.024>.
- [57] Aizawa T, Bin Abdullah MFE, Inoue A, Ishidzuka Y, Taki N, Kosaka H. Aromatic additive effects on soot formation in a fischer-tropsch diesel (FTD) spray flame via laser spectroscopy. *Proc. 8th Int. Conf. Model. Diagnostics Adv. Engine Syst. COMODIA 2012*, 2012, p. 275–80.
- [58] Aizawa T, Takahata N, Okabe K, Mizutani Y. Effect of Fuel Aromatics on In-Flame Diesel Soot Nanostructure via HRTEM. *SAE Tech Pap* 2015;2015-Sept. <https://doi.org/10.4271/2015-01-1829>.
- [59] Miyamoto N, Ogawa H, Shibuya M. Distinguishing the effects of aromatic content and ignitability of fuels in diesel combustion and emissions. *SAE Tech Pap* 1991. <https://doi.org/10.4271/912355>.
- [60] Reijnders J, Boot M, de Goey P. Impact of aromaticity and cetane number on the soot-NOx trade-off in conventional and low temperature combustion. *Fuel* 2016;186:24–34. <https://doi.org/10.1016/j.fuel.2016.08.009>.
- [61] Herreros JM, Jones A, Sukjit E, Tsolakis A. Blending lignin-derived oxygenate in

- enhanced multi-component diesel fuel for improved emissions. *Appl Energy* 2014;116:58–65. <https://doi.org/10.1016/j.apenergy.2013.11.022>.
- [62] Han M. The effects of synthetically designed diesel fuel properties - Cetane number, aromatic content, distillation temperature, on low-temperature diesel combustion. *Fuel* 2013;109:512–9. <https://doi.org/10.1016/j.fuel.2013.03.039>.
- [63] Ladommatos N, Xiao Z, Zhao H. Effects of fuels with a low aromatic content on diesel engine exhaust emissions. *Proc Inst Mech Eng Part D J Automob Eng* 2000;214:779–94. <https://doi.org/10.1243/0954407001527646>.
- [64] Kidoguchi Y, Yang C, Miwa K. Effects of fuel properties on combustion and emission characteristics of a direct-injection diesel engine. *SAE Tech Pap* 2000;109:1149–57. <https://doi.org/10.4271/2000-01-1851>.
- [65] Takahashi S, Wakimoto K, Iida N, Nikolic D. Effects of aromatics content and 90% distillation temperature of diesel fuels on flame temperature and soot formation. *SAE Tech Pap* 2001. <https://doi.org/10.4271/2001-01-1940>.
- [66] Wang H, Yao M, Yue Z, Jia M, Reitz RD. A reduced toluene reference fuel chemical kinetic mechanism for combustion and polycyclic-aromatic hydrocarbon predictions. *Combust Flame* 2015;162:2390–404. <https://doi.org/10.1016/j.combustflame.2015.02.005>.
- [67] Xu Z, Duan X, Liu Y, Deng B, Liu J. Spray combustion and soot formation characteristics of the acetone-butanol-ethanol/diesel blends under diesel engine-relevant conditions. *Fuel* 2020;280:118483. <https://doi.org/10.1016/j.fuel.2020.118483>.
- [68] Qian Y, Qiu Y, Zhang Y, Lu X. Effects of different aromatics blended with diesel on combustion and emission characteristics with a common rail diesel engine. *Appl Therm Eng* 2017;125:1530–8. <https://doi.org/10.1016/j.applthermaleng.2017.07.145>.
- [69] Kook S, Pickett LM. Liquid length and vapor penetration of conventional, Fischer-Tropsch, coal-derived, and surrogate fuel sprays at high-temperature and high-pressure ambient conditions. *Fuel* 2012;93:539–48.

<https://doi.org/10.1016/j.fuel.2011.10.004>.

- [70] Butts RT, Foster D, Krieger R, Andrie M, Ra Y. Investigation of the effects of cetane number, volatility, and total aromatic content on highly-dilute low temperature diesel combustion. SAE Tech Pap 2010. <https://doi.org/10.4271/2010-01-0337>.
- [71] Abu-Jrai A, Rodríguez-Fernández J, Tsolakis A, Megaritis A, Theinnoi K, Cracknell RF, et al. Performance, combustion and emissions of a diesel engine operated with reformed EGR. Comparison of diesel and GTL fuelling. *Fuel* 2009;88:1031–41. <https://doi.org/10.1016/j.fuel.2008.12.001>.
- [72] Barbella R, Ciajolo A, D’Anna A, Bertoli C. Effect of fuel aromaticity on diesel emissions. *Combust Flame* 1989;77:267–77. [https://doi.org/10.1016/0010-2180\(89\)90134-X](https://doi.org/10.1016/0010-2180(89)90134-X).
- [73] de Ojeda W, Bulicz T, Han X, Zheng M, Cornforth F. Impact of Fuel Properties on Diesel Low Temperature Combustion. *SAE Int J Engines* 2011;4:188–201. <https://doi.org/10.4271/2011-01-0329>.
- [74] Rao L, Zhang Y, Kook S, Kim KS, Kweon CB. Morphology and internal structure of soot particles under the influence of jet–swirl and jet–jet interactions in a diesel combustion environment. *Combust Flame* 2020;214:25–36. <https://doi.org/10.1016/j.combustflame.2019.12.017>.
- [75] Zhang Y, Zhang R, Rao L, Kim D, Kook S. The influence of a large methyl ester on in-flame soot particle structures in a small-bore diesel engine. *Fuel* 2017;194:423–35. <https://doi.org/10.1016/j.fuel.2017.01.044>.
- [76] Song J, Alam M, Boehman AL, Kim U. Examination of the oxidation behavior of biodiesel soot. *Combust Flame* 2006;146:589–604. <https://doi.org/10.1016/j.combustflame.2006.06.010>.
- [77] Lamharess N, Millet CN, Starck L, Jeudy E, Lavy J, Da Costa P. Catalysed diesel particulate filter: Study of the reactivity of soot arising from biodiesel combustion. *Catal. Today*, vol. 176, Elsevier; 2011, p. 219–24. <https://doi.org/10.1016/j.cattod.2011.01.011>.

- [78] Zhang R, Pham PX, Kook S, Masri AR. Influence of biodiesel carbon chain length on in-cylinder soot processes in a small bore optical diesel engine. *Fuel* 2019;235:1184–94. <https://doi.org/10.1016/j.fuel.2018.08.096>.
- [79] Goyal H, Zhang Y, Kook S, Kim KS, Kweon CB. Low- to High-Temperature Reaction Transition in a Small-Bore Optical Gasoline Compression Ignition (GCI) Engine. *SAE Int J Engines* 2019;12:473–88. <https://doi.org/10.4271/03-12-05-0031>.
- [80] Pickett LM, Siebers DL. Soot in diesel fuel jets: Effects of ambient temperature, ambient density, and injection pressure. *Combust Flame* 2004;138:114–35. <https://doi.org/10.1016/j.combustflame.2004.04.006>.
- [81] Cenker E, Bruneaux G, Pickett L, Schulz C. Study of soot formation and oxidation in the engine combustion network (ECN), spray A: Effects of ambient temperature and oxygen concentration. *SAE Int J Engines* 2013;6:352–65. <https://doi.org/10.4271/2013-01-0901>.
- [82] Zhang J, Jing W, Roberts WL, Fang T. Soot measurements for diesel and biodiesel spray combustion under high temperature highly diluted ambient conditions. *Fuel* 2014;135:340–51. <https://doi.org/10.1016/j.fuel.2014.06.071>.
- [83] Min K, Valco DJ, Oldani A, Kim K, Temme J, Kweon CBM, et al. Autoignition of varied cetane number fuels at low temperatures. *Proc Combust Inst* 2019;37:5003–11. <https://doi.org/10.1016/j.proci.2018.05.078>.
- [84] Kondo K, Kuribayashi M, Sakai K, Aizawa T. High-speed ultraviolet chemiluminescence imaging of late combustion in diesel spray flame. *Int J Engine Res* 2017;18:93–104. <https://doi.org/10.1177/1468087416684065>.
- [85] O'Connor J, Musculus M. Post injections for soot reduction in diesel engines: A review of current understanding. *SAE Int J Engines* 2013;6:400–21. <https://doi.org/10.4271/2013-01-0917>.
- [86] Dec JE, Espey C. Ignition and early soot formation in a di diesel engine using multiple 2-D imaging diagnostics. *SAE Tech Pap* 1995;104:853–75. <https://doi.org/10.4271/950456>.

- [87] Dec JE, Espey C. Chemiluminescence imaging of autoignition in a DI diesel engine. SAE Tech Pap 1998;107:2230–54. <https://doi.org/10.4271/982685>.
- [88] Rusly AM, Le MK, Kook S, Hawkes ER. The shortening of lift-off length associated with jet-wall and jet-jet interaction in a small-bore optical diesel engine. Fuel 2014;125:1–14. <https://doi.org/10.1016/j.fuel.2014.02.004>.
- [89] Le MK, Zhang R, Rao L, Kook S, Hawkes ER. The development of hydroxyl and soot in a methyl decanoate-fuelled automotive-size optical diesel engine. Fuel 2016;166:320–32. <https://doi.org/10.1016/j.fuel.2015.11.006>.
- [90] Musculus MPB. Multiple simultaneous optical diagnostic imaging of early-injection low-temperature combustion in a heavy-duty diesel engine. SAE Tech Pap 2006;2006. <https://doi.org/10.4271/2006-01-0079>.
- [91] Genzale CL, Reitz RD, Musculus MPB. Optical diagnostics and multi-dimensional modeling of spray targeting effects in late-injection low-temperature diesel combustion. SAE Int J Engines 2010;2:150–72. <https://doi.org/10.4271/2009-01-2699>.
- [92] Brackmann C, Nygren J, Bai X, Li Z, Bladh H, Axelsson B, et al. Laser-induced fluorescence of formaldehyde in combustion using third harmonic Nd:YAG laser excitation. Spectrochim Acta - Part A Mol Biomol Spectrosc 2003;59:3347–56. [https://doi.org/10.1016/S1386-1425\(03\)00163-X](https://doi.org/10.1016/S1386-1425(03)00163-X).
- [93] Zhang Y, Tian R, Meng S, Kook S, Kim KS, Kweon C-B. Effect of the jet fuel cetane number on combustion in a small-bore compression-ignition engine. Fuel 2021;292:120301. <https://doi.org/10.1016/j.fuel.2021.120301>.
- [94] Le MK, Kook S, Hawkes ER. The planar imaging of laser induced fluorescence of fuel and hydroxyl for a wall-interacting jet in a single-cylinder, automotive-size, optically accessible diesel engine. Fuel 2015;140:143–55. <https://doi.org/10.1016/j.fuel.2014.09.089>.
- [95] Tian R, Zhang Y, Kook S, Kim KS, Kweon C-B. Effect of jet fuel aromatics on in-flame soot distribution and particle morphology in a small-bore compression ignition engine. Fuel 2021;305:121582.

<https://doi.org/10.1016/j.fuel.2021.121582>.

- [96] Tian R, Zhang Y, Kook S. On-grid location-by-location variations of transmission electron microscope imaged in-flame soot particles in a small-bore diesel engine. 22nd Australas. Fluid Mech. Conf. AFMC2020, University of Queensland Library; 2020. <https://doi.org/10.14264/0c89481>.
- [97] Gao Y, Kim D, Zhang YL, Kook S, Xu M. Influence of ethanol blending ratios on in-flame soot particle structures in an optical spark-ignition direct-injection engine. *Fuel* 2019;248:16–26. <https://doi.org/10.1016/j.fuel.2019.02.131>.
- [98] Kondo K, Aizawa T, Kook S, Pickett L. Uncertainty in Sampling and TEM Analysis of Soot Particles in Diesel Spray Flame. SAE Tech Pap 2013;2013-April. <https://doi.org/10.4271/2013-01-0908>.
- [99] Le MK, Zhang Y, Zhang R, Rao L, Kook S, Chan QN, et al. Effect of jet-jet interactions on soot formation in a small-bore diesel engine. *Proc Combust Inst* 2017;36:3559–66. <https://doi.org/10.1016/j.proci.2016.07.025>.
- [100] Zhang YL, Zhang R, Kook S. Nanostructure Analysis of In-flame Soot Particles under the Influence of Jet-Jet Interactions in a Light-Duty Diesel Engine. *SAE Int J Engines* 2015;8. <https://doi.org/10.4271/2015-24-2444>.
- [101] O'Connor J, Musculus M. Optical investigation of the reduction of unburned hydrocarbons using close-coupled post injections at LTC conditions in a heavy-duty diesel engine. *SAE Int J Engines* 2013;6:379–99. <https://doi.org/10.4271/2013-01-0910>.
- [102] Kosaka H, Aizawa T, Kamimoto T. Two-dimensional imaging of ignition and soot formation processes in a diesel flame. *Int J Engine Res* 2005;6:21–42. <https://doi.org/10.1243/146808705X7347>.
- [103] Miyashita K, Fukuda Y, Shiozaki Y, Kondo K, Aizawa T, Yoshikawa D, et al. TEM Analysis of Soot Particles Sampled from Gasoline Direction Injection Engine Exhaust at Different Fuel Injection Timings. SAE Tech Pap 2015;2015-Sept. <https://doi.org/10.4271/2015-01-1872>.

- [104] Hurt RH, Crawford GP, Shim HS. Equilibrium nanostructure of primary soot particles. *Proc Combust Inst* 2000;28:2539–46. [https://doi.org/10.1016/S0082-0784\(00\)80670-0](https://doi.org/10.1016/S0082-0784(00)80670-0).
- [105] Ishiguro T, Takatori Y, Akihama K. Microstructure of diesel soot particles probed by electron microscopy: First observation of inner core and outer shell. *Combust Flame* 1997;108:231–4. [https://doi.org/10.1016/S0010-2180\(96\)00206-4](https://doi.org/10.1016/S0010-2180(96)00206-4).
- [106] Su HC, Kook S, Chan QN, Hawkes ER, Le MK, Ikeda Y. A comparison of high-temperature reaction and soot processes of conventional diesel and methyl decanoate. *Fuel* 2018;226:635–43. <https://doi.org/10.1016/j.fuel.2018.04.051>.